Effect of rGO on the Microstructure and Thermoelectric Properties of $SnSe_2$ for Green Energy Harvesting

Name: Haad Khan

Reg. No.: 00000205713

This thesis is submitted as a partial fulfillment of the requirements for the degree of

MS (Materials and Surface Engineering)

Supervisor: Dr. Muhammad Siyar

School of Chemical and Materials Engineering (SCME)

National University of Sciences and Technology (NUST)

H-12 Islamabad, Pakistan

August, 2021

Dedication

I would like to dedicate this thesis to the martyrs of Army Public School, Peshawar, and Abdul Sattar Edhi, a humanitarian, who once lived.

Acknowledgements

“And HE found you lost, and guided you.” [Al-Qur’an, 93:7]

It is a genuine pleasure to express my gratitude to my mentor and a very understanding teacher, my supervisor, **Dr. Muhammad Siyar**. Without his unconditional support and valuable guidance, this research would never have been possible. I also want to express my gratitude to my GEC members, **Dr. Khurram Yaqoob**, **Dr. I. H. Gul** and **Dr. Aftab Akram**, who were supportive at all times and guided me throughout my research.

I would like to extend my gratitude towards Principal, SCME; **Dr. Amir Azam Khan** and the HoD, Materials Engg. Dept.; **Dr. Zakir Hussain** for their constant support and guidance throughout my tenure at SCME and during the research as well. I would also like to thank Dr. Jameel-ur-Rehman from Oslo University, Norway, for helping me in studying and evaluating the thermoelectric properties.

Secondly, I would like to appreciate the persistent help that was provided by **Maroosha Farid**, my fellow MS student.

Moreover, I would like to express my sincerest thanks to all the faculty member and non-teaching staff. I would like to mention **Lab Engr. Zeeshan Qureshi** and **Engr. Muhammad Zafar Khan** for their constant assistance during the lab work.

Last but not the least, I want to thank my parents, my better half, my siblings and all the people whose assistance and support was a milestone in the completion of this project.

~ Haad Khan

Abstract

Thermoelectric (TE), is a solid-state technology to convert waste heat into useful energy based on Seebeck effect, which can make significant contributions to solve the global energy crisis by providing a sustainable energy solution. SnSe, being a lead-free, environmentally friendly and cheap semiconductor, has been an attractive choice for TE community. Here, the focus is on its layered structure of the same chalcogenide family, $SnSe_2$, an n-type semiconductor. In this research, we analyzed the potential of $SnSe_2$-rGO composite as a TE material and the effect of rGO concentration on its TE properties. $SnSe_2$-rGO composites were synthesized via solvothermal route followed by sintering at 550°C in the presence of Argon. In-situ doping of rGO within $SnSe_2$ matrix was successfully achieved. The resultant composite showed a significant improvement in electrical conductivity which displayed a peak value of 2479 S/m (Pure $SnSe_2$=750 S/m) at 300K. This enhancement is due to the electronic structure of $SnSe_2$ and the presence of rGO conductive sheets, which improved the carrier concentration. Introduction of rGO also resulted in controlling the lattice thermal conductivity due to phonon scattering. The investigation showed that increasing the rGO concentration had a positive impact on the overall ZT of the samples, achieving a peak ZT of 0.18 for 4-SG sample at 750K. This increase can be related to the increasing electrical conductivity due to rGO addition and the reduction in band gap.

Table of Contents

List of Figures

List of Tables

Abbreviations

IRENA: International Renewable Energy Agency

TE: Thermoelectric

TEG: Thermoelectric Generator

MFP: Mean Free Path

XRD: X-ray Diffractometer

SEM: Scanning Electron Microscope

LFA: Laser Flash Analysis

UV-Vis: UV-Visible

TC: Thermocouple

PVP: Polyvinylpyrrolidone

GO: Graphene Oxide

rGO: Reduced Graphene Oxide

CHAPTER 1 INTRODUCTION

1.1 Background

The technology developments around the globe in the field of energy are drastic and with each passing day, the focus towards green energy is increasing as green energy harvesting is the future due to its environmental friendliness. Given the current environmental, economic and security concerns linked to fossil fuels, it has become vital to move towards sustainable resources of energy conversion and storage. It has become important now to improve energy efficiency and reduce the power consumption. The advancements in the technologies by the civilizations has resulted in increased environmental pollution and as a consequence of that, it now demands alternative sources of energy. Consequently, the search for green energy keeps on evolving and growing.

In recent times, fossil fuels' consumption has affected the global climate. During the last decade, carbon dioxide footprint has reached record levels and that is alarming for the world [1-3]. Scientific research has proposed, there is a dire need to develop concerted policies, in order to prevent the world and its environment from catastrophic circumstances [8]. One possible way to avoid the catastrophe is to reduce the ever-increasing energy demand via increased efficiency along with conservation of the harvested energy. Secondly, to fulfill the energy challenges in the future, development of a wider range of renewable energy resources is of paramount importance [2]. The existing revolutionary technologies for renewable energy such as wind, solar, biomass, etc. should be further enhanced and developed [9].

1.2 World Energy Statistics

According to International Renewable Energy Agency (IRENA), in 2017, energy consumption around the globe was 13-billion-ton oil equivalent (toe). IRENA forecasted that by 2035, this figure will reach 18 billion toe.

The report by IRENA also indicates that currently, coal is the most widely used fuel for energy production. Coal has a giant carbon footprint and that makes it dangerous for the environment. As a result, the world is moving towards renewable energy resources and according to IRENA, renewable energy resources will be replacing coal as the most widely used resource of energy, by 2035 [96]. Figure 1.1 illustrates the comparison of consumption of different energy resources between 1994-2017 and 2017-2035. The figure also shows that the consumption of renewable energy resources is increasing as the world is moving towards an environmentally friendly future.

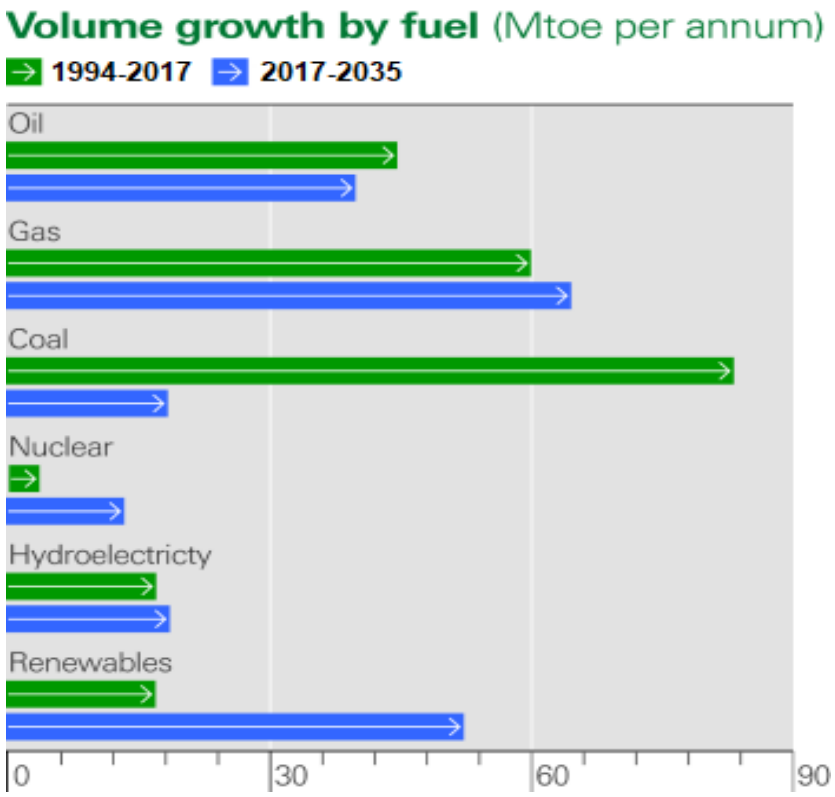

Figure 1.1 Volume Growth of Fuel [97]

1.3 Thermoelectric (TE) Materials

Thermoelectric materials, although have been around for many years, are a convenient source for conversion of waste heat into useful power [6,7]. In recent years, TE materials are becoming an area of prime focus when it comes to alternate energy resources due to their quality of interconversion of heat and electricity [10]. Thermoelectric generators

(TEG) are known for their ability to extract electrical energy from waste heat. There are multiple advantages of TEGs such as: compact structure, direct interconversion in solid state, noise-free operation, absence of moving parts, absence of perilous working fluids [11-14]. However, the availability of TEGs is very limited currently, due to their high cost and lower efficiency compared to the other renewable energy resources [15]. Therefore, the need for efficiency enhancement of TE materials as well as exploring TE materials with lower costs is of prime importance. The efficiency of TE materials can be improved via composite approaches using novel compositions and innovative designs [16].

1.3.1 Application of TE Devices

TE devices are getting increasing attention as alternate and sustainable energy resources. Also, as the electronic circuits and sensors are getting smaller in size, the issues relating to heat management are a becoming a challenge and often cause failure, for such case, TE devices are a suitable solution [17,18]. Second important application of TE materials can be in power generation where TEGs can be used, as they convert waste heat into electric power [19]. In the process of combustion, energy in excess of 60% is lost according to the research. This energy loss is huge and as a result, it causes not only low efficiency but a negative impact on the environment as well. One of the prime industries that can benefit from TE devices is the automotive industry as TE materials can be used to extract the heat that goes as a waste, from the exhaust of an automobile and convert that into useful power. This extracted power can be used for seat warming, charging the battery of the car or powering other electronic parts of the automobile [20,21]. This approach will ultimately not only enhance efficiency, but also, reduce the environmental impact that is resulted from this waste heat.

TEGs can be used for utilizing the waste heat resulting from human body as well, in order to power small electronic devices like a wristwatch as it only requires 20-40 μW. Watch manufacturers like Citizen and Seiko have already installed TEGs on their watches to use the waste heat for energizing their watches [22]. TEGs also have a utility when it comes to implants in human body as they can be used for powering medical devices. Around the globe, many of the industries use heavy duty furnaces which require high temperatures

and as a result, they release the waste heat in the form of exhaust gases through the chimney. This wasted heat can be recovered through TEGs and can be used for various other electrical applications and can also reduce the impact on our environment [23].

1.3.2 Advantages of TE Materials

TE materials, although have not gained wide acceptance yet, have the capability of becoming one of the most widely used renewable energy resource as the major phenomenon of TE materials is to recover the waste heat. The field of TE materials is not populated yet and there is a limited number of options that can be considered for TE applications. Researchers are working on enhancing the TE properties of the existing materials and are trying to explore new options for TE applications as the future belongs to renewable energy resources and TE materials are an important part of that. Research shows us that the ZT or the figure of merit of TE materials has shown improvement over time, with the advancements in the field of science and with more research, it can reach an acceptable value where TE materials can then be used for industrial applications, in recovering the waste heat and in turn, improving the overall efficiency of an industry [28].

TE materials have various advantages compared to conventional renewable energy resources including, high reliability, compact size, no moving parts, lightweight, powered by waste heat or direct current, no fluids involved, high scalability, and easy to switch between heating and cooling modes [28]. Apart from this, TE materials are also environmentally friendly, as in, they are not hazardous to the environment and are noise-free as well [28].

1.4 Thermoelectric Effects

The temperature gradient that exists across a thermoelectric material results in generation of electricity – electrons and holes (charge carriers) diffuse at the hot junction and move towards the cold junction, resulting in movement of charge and/or electric current. This behavior can be attributed to the higher energy level across the hot source [24]. As a result of this charge difference that is built up among the hot side and the cold side, a voltage is

produced and subsequently, electric current. TE effect basically follows the fundamental phenomena of Physics [10].

1.4.1 Seebeck Effect

Nearly 200 years ago, the phenomenon of thermoelectricity was discovered. Thomas Seebeck, in 1821, discovered that if there exists a temperature gradient between two different types of conductors, there will appear a voltage drop across the circuit. This concept is now known as Seebeck effect and it has great application when it comes to generating thermal power [1,2].

Mathematically, Seebeck effect can be represented as:

$$S = \frac{-\Delta V}{\Delta T}$$

Where S represents Seebeck coefficient, ΔV represents the difference in voltage, and ΔT represents the temperature gradient between the two junctions. For an n-type semiconductor, Seebeck coefficient has a negative value, where the electrons disperse from the hot source towards the cold source; and for a p-type semiconductor, the phenomenon reverses, as the holes move from hot source towards the cold and the value of Seebeck in such case would be positive [24,25].

1.4.2 Peltier Effect

The reverse phenomenon to Seebeck effect was discovered by Jean Peltier. In 1834, Peltier discovered that when current is allowed to pass through the junction of point of two dissimilar conductors, a resultant heat may be removed or generated at the junction. This discovery is named after Jean Peltier, known as Peltier effect [1,3].

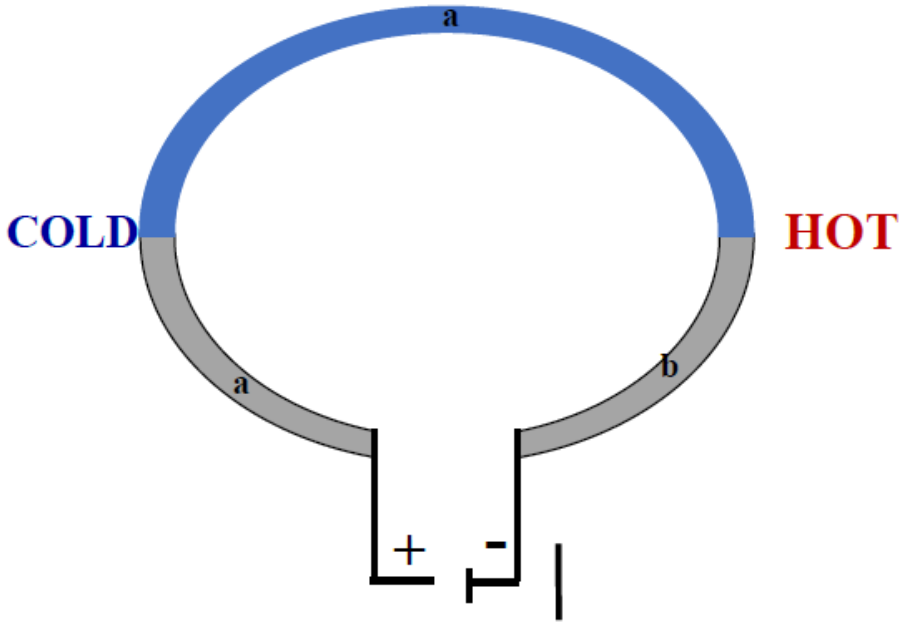

Figure 1.2 Demonstration of Peltier Effect [49]

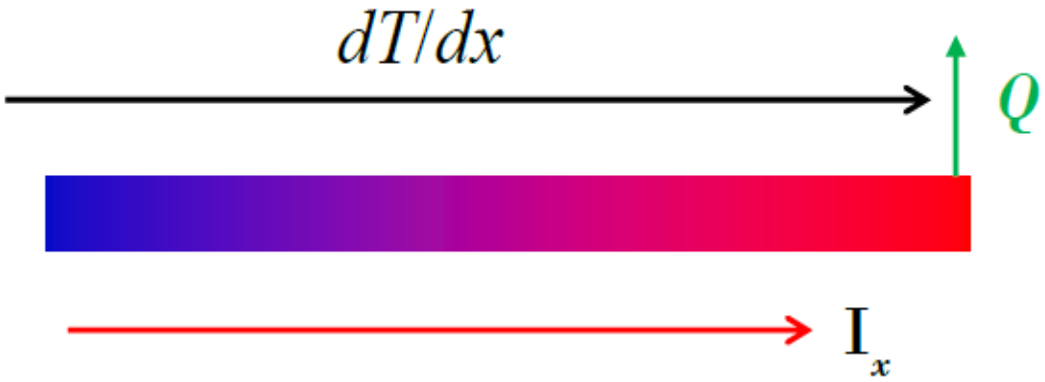

Figure 1.3 Demonstration of Thomson Effect [50]

The mathematical representation for calculating the Peltier heat at the junction is as follows:

$Q = \pi.I$

Where *Q* represents absorbed heat and is directly related to I and π, which represent current and Peltier coefficient, respectively [10]. Lentz, in 1838, further explained the phenomenon of Peltier effect – when electric current passes through a circuit, heat energy is either generated or absorbed [5]. Figure 1.2 illustrates the basic working phenomenon of Peltier effect.

1.4.3 Thomson Effect

Later, Lord Kelvin, in 1851, studied the correlation between the Peltier effect and the Seebeck effect and it is known as the Thomson effect. He analyzed this relationship by application of thermodynamic theory to the problem at hand and then suggested that for a homogenous conductor, there has to exist a third effect – when an electric current pass through a uniform electrical conductor that has a temperature gradient, the resultant can be release or absorption of not only irreversible Joule heat but also reversible heat [4,5]. The three effects discussed above, form the theoretical framework that is the basis of thermoelectricity. Figure 1.3 illustrates the working phenomenon of Thomson Effect.

1.4.4 Figure of Merit

The figure of merit or ZT is used for determining the conversion efficiency of the thermoelectric materials [26], and it can be represented as follows:

$$ZT = \frac{S^2 \sigma T}{\kappa}$$

In this relation, S represents Seebeck coefficient, σ represents electrical conductivity, κ represents thermal conductivity, and T represent temperature. S^2 σ combined, represents power factor or PF and a higher value of PF gives rise to higher current and higher voltage generation which is desired. According to this relation, to maximize ZT value, high value of electrical conductivity is required, along with high value of Seebeck coefficient but at

the same time, low thermal conductivity. Nonetheless, κ has two components, the electronic thermal conductivity (κ_{el}) and the lattice thermal conductivity (κ_{latt}). consequently, $\kappa = \kappa_{el} + \kappa_{latt}$. According to recent studies, it is reported that if lattice thermal conductivity is reduced, the overall value of κ reduces and as a result, ZT improves [10,12,24].

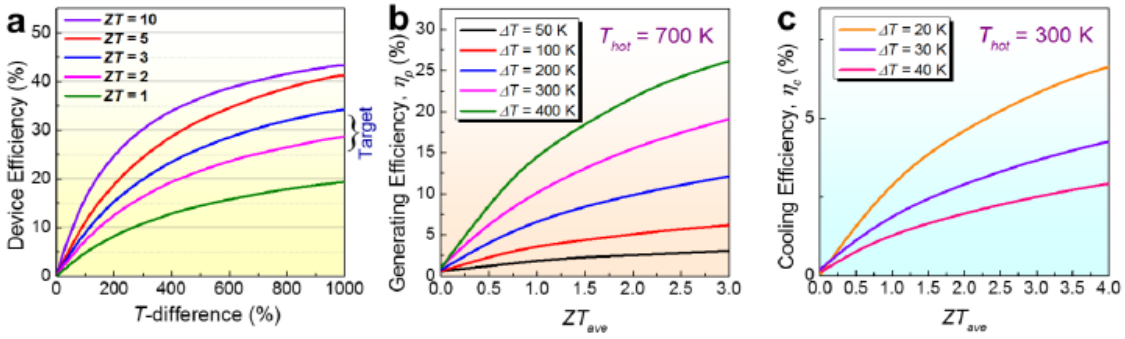

Figure 1.4 (a) Efficiency of TE devices as a function of ΔT [47] **(b)** Power Generation Efficiency and **(c)** Refrigeration efficiency as function of ZT_{avg} [48]

For TE materials, it is important that they have a high value of ZT as it is their figure of merit and determines their efficiency. Figure 1.4 illustrates the relationship between ZT and different parameters. Figure 1.4 (a) illustrates the relationship between the TE efficiency and the ΔT. It can be seen from the figure that the higher ZT results in a higher efficiency. At the ZT value of 2, the efficiency can surpass 15% which is the efficiency of a typical engine and that makes it evident that TE materials can become better performers over time. Figure 1.4 (b) illustrates the relationship between ZT and the generated efficiency and it portrays that the efficiency increases with the increasing temperatures. Similarly, the opposite of this can be seen in Figure 1.4 (c) where ZT is plotted against cooling efficiency and it can be seen that the efficiency increases with the decreasing temperature. Overall, Figure 1.4 illustrates the effect of different scenarios on the ZT value.

1.5 n-type and p-type TE Materials

Thermoelectric devices exist in the form of thermocouple, consisting of an n-type material and a p-type material. Material with negative charge carriers (electrons) as the dominant charge is referred to as n-type material while the one with positive free charge carriers (holes) as the dominant charge are termed as p-type materials. Figure 1.5 (a) highlights a schematic of TEG while Figure 1.5 (b) highlights the schematic for Peltier refrigeration model. In TEG module, the voltage difference, which is proportional to the temperature difference, will cause current flow, generating electric power. This electric power is the product of electrical current and the voltage across the hot side and the cold side [27]. Due to the resistance of thermoelectric materials, TEGs possess internal resistance. When load is decreased, this internal resistance, may cause a drop in the voltage. However, when the load and the internal resistance are almost equated, maximum efficiency can be achieved as this helps provide the maximum power from the load [27].

In the refrigeration module, load application is through an external source such as a battery, which then drives the heat via free charge carriers (holes and/or electrons) from one side to the other side [25,27]. Peltier device's efficiency is also dependent on the efficiency of the TE materials as a larger ZT value will result in enhanced efficiency of the TE materials [27].

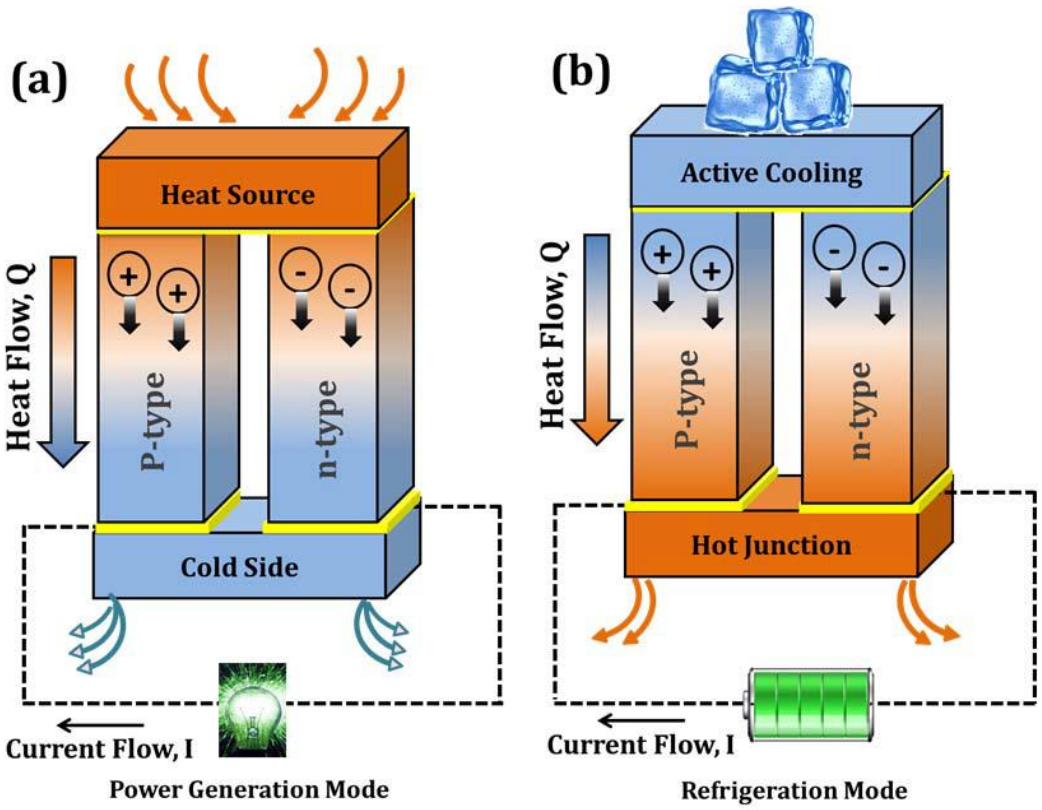

Figure 1.5 Schematic Illustration of TE devices **(a)** TEG Module, **(b)** Refrigeration Module [27]

1.6 Challenges in Thermoelectric Research

For improved TE properties, it is of prime importance that the ZT value is improved. During the last decade, the improvement has been marginal [12]. Unfortunately, no single available material in nature has come out as a good TE candidate. There are always shortcomings in some area. The major concern or challenge is the three interrelated properties that are used to quantify ZT, i.e. σ, S *and* κ. For a higher value of ZT, it is important that S and σ have a high value while κ should have a lower value [24]. Their dependence on each other has hindered the advancement and has left us with a limited number of materials that can be considered for TE applications [12]. Figure 1.6 shows the relationship between the abovementioned interrelated properties.

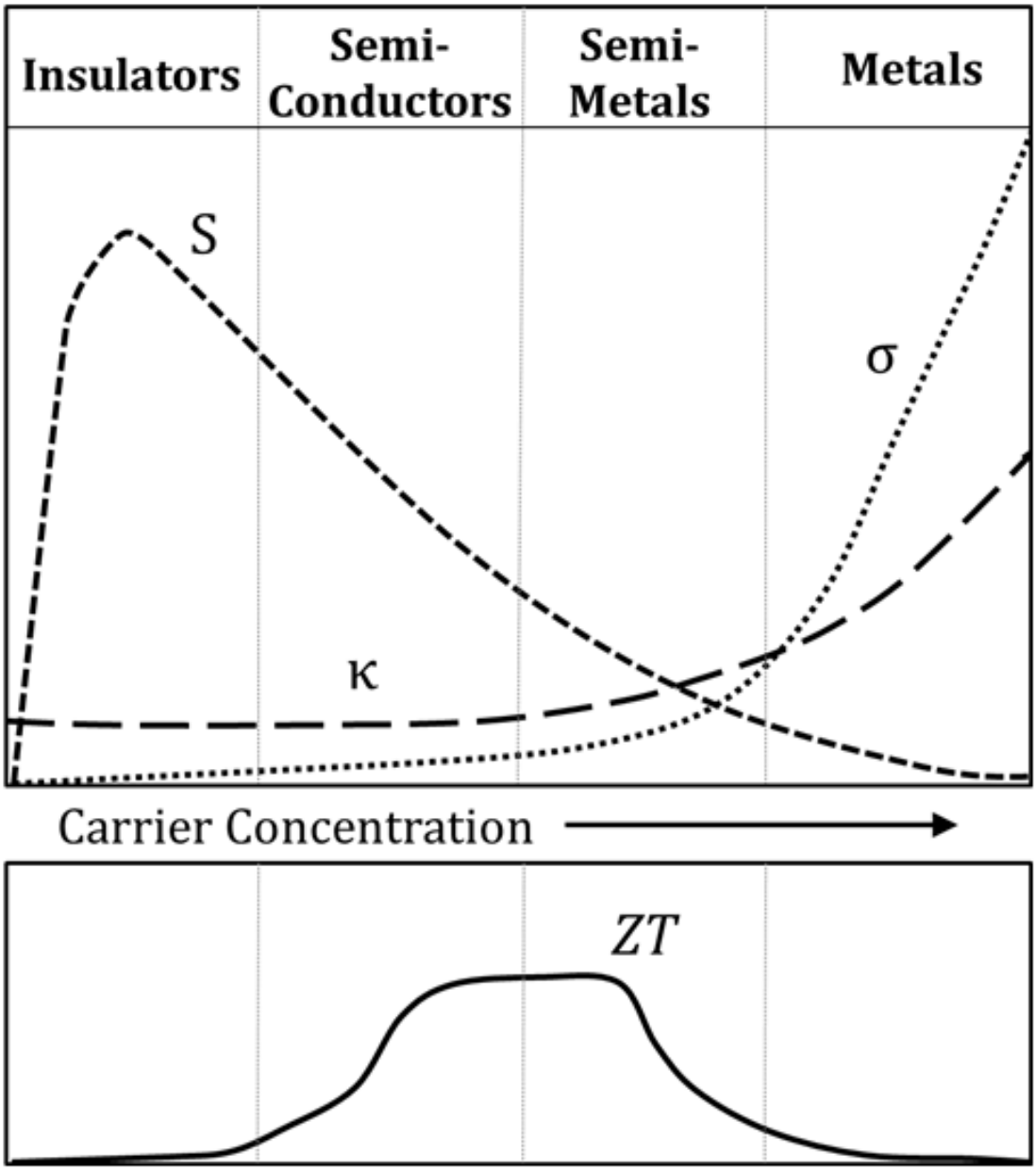

Figure 1.6 Thermoelectric behavior of various classes of materials [14]

It can be seen from Figure 1.6 that metals possess a high σ and κ but has a low Seebeck coefficient (S). As a result, the ZT value remains low. Insulators have poor electrical and thermal conductivity, so they are not suitable for TE applications. In the middle of the graph, the semiconductors and the semi-metals display a relatively higher σ value and

lower κ and therefore, this class of materials can lead to an enhanced and optimum value of ZT [12].

Upon integration of TE materials into devices, a set of challenges arise for instance, coupling of n- and p-type materials with ceramic plates, metallic contacts and the thermal expansion coefficient of materials. These parameters are of major concern in designing a TE device [10]. In some cases, packaging too becomes an issue as sometimes, TE materials are air sensitive and hence, require an inert atmosphere to be operational. Similarly, the tubular or planar design preference is also a parameter of consideration and it depends on the desired application [10].

1.7 Objectives of the Study

The prime objective of this research work is to find a TE material that is lead-free and cheap, and then improve the properties of such TE material. One promising option that can be analyzed is SnSe-based TE materials. The compound selected for the purpose of this research is tin diselenide ($SnSe_2$). The investigation will be focused on enhancing the TE properties of $SnSe_2$ by introducing graphene into the structure, making it a composite. Once the $SnSe_2$-rGO composite is obtained, it will then be analyzed for TE properties.

CHAPTER 2 LITERATURE REVIEW

2.1 Strategies to Improve TE Properties

Improving the TE properties of $SnSe_2$ is of prime concern in this research. There can be multiple approaches to enhancing the TE properties of $SnSe_2$ and some of those approaches are discussed below:

2.1.1 Enhancing Carrier Concentration

Enhancing the carrier concentration is one of the routes that can be adopted for improving the ZT of $SnSe_2$ based TE materials. The optimum value of carrier concentration ranges between 10^{19} and 10^{21} [14]. If the carrier concentration value lies between the said range, optimum level of power factor can be achieved. To enhance the carrier concentration, there are generally two ways that are considered which are extrinsic doping and fine-tuning of intrinsic defects.

2.1.1.1 Extrinsic Doping

This can be achieved through multiple routes, but the most common way is alloying with neighboring column elements in the periodic table [30,31]. It should be noted that even though, this technique seems fairly simple, selecting a suitable dopant is not a simple thing. In some special cases, the optimum value for carrier concentration is not achieved and the reason is the dopant's doping efficiency and the solubility limit, and due to this reason, the theoretically acclaimed efficiency is not achieved practically [32,33]. Furthermore, in semiconductors constituting of 2 or more elements, it becomes difficult to control the dopant's solubility due to the presence of a new elemental specie.

2.1.1.2 Tuning Intrinsic Defects

There exist intrinsic defects in the structure of semiconductors which include but are not limited to, interstitials, antisites and vacancies. These defects lower the efficiency of the

TE materials and hence, should be improved in order to attain a better efficiency. The concentration and types of these point defects are highly dependent on the composition of the compound and can be controlled through extrinsic doping. As a general example, a smaller difference of covalent radius and electronegativity between the anion and the cation will give rise to antisite defects in cation, and if the difference is bigger, it will result in vacancy formation in the anion [34,35].

2.1.1.3 Carrier Mobility

Along with carrier concentration, it is also of prime importance that the carrier mobility is also improved as the transport of electron depends upon carrier mobility and in this way, electrical conductivity of the resultant compound can be improved for better TE properties [34].

2.1.2 Reducing Thermal Conductivity

Reduction of thermal conductivity or κ is also an important parameter as it can help enhance the ZT of the subject TE material. The total thermal conductivity, as discussed in section 1.4.4, is the sum of lattice thermal conductivity and electronic thermal conductivity or $\kappa = \kappa_{el} + \kappa_{latt}$. Wiedemann-Franz law is used for calculating the electronic thermal conductivity i.e. $\kappa_{el} = L\sigma T$, where L is Lorenz parameter, and its value remains between the range of 1.6 and 2.5 x $W\Omega K^{-2}$ [36,37]. According to Wiedemann-Franz law, with electrical conductivity, the value of κ_{el} also increases and the increase is linear in nature. Therefore, it is important that a suitable carrier concentration is provided, for a better performing TE material [38,39].

2.1.2.1 Point Defects

Introducing point defects is an effective strategy to introduce lattice imperfections with a length scale of a unit cell at most, or one interatomic distance. These defects can be

introduced through vacancies, interstitials, and substitutions [40]. As discussed in section 2.1.1.2, these point defects can affect the overall ZT.

Callaway and Klemens developed a thermal conductivity model and according to that, MFP (mean free path) phonons are scattered by point defects which is related to either the local bond strain that is introduced due to the defects or the mass contrast, and this all is controlled by the scattering parameter or Γ [44,45]. The expression for Γ is as follows:

$$\Gamma = \mathrm{x}(1-\mathrm{x})\left[\left(\frac{\Delta \mathrm{M}}{M}\right)^2 + \varepsilon\left(\frac{a_{disorder} - a_{pure}}{a_{pure}}\right)^2\right]$$

In the above expression, x represents the doping fraction, $a_{disorder}$ and a_{pure} are disordered and pure alloys' lattice constants, respectively. $\Delta M/M$ represents the change in atomic mass and $\boldsymbol{\varepsilon}$ represents the adjustment parameter related to the elastic property [46].

2.1.2.2 Nanostructuring

Nanostructuring is another way to reduce thermal conductivity and it can be either achieved through nanoscale particles for a single phase or through embedment of nanoscale precipitates within the matrix for a solid solution [41]. Through mechanical methods like ball milling or melt-spinning, one can achieve nanoscale particles [42,43]. However, quenching of an extensively doped solid solution is the preferred technique for achieving second phase precipitation. It should be noted that for the second phase precipitate, the solubility in the solid solution should be low or completely absent, but for liquid state, it should be completely soluble [41].

2.1.2.3 Compromise Between κ and μ

There's always a compromise between carrier mobility (μ) and thermal conductivity of the lattice (κ_{lat}). The introduction of nanostructuring, point defects, dislocations, etc. which are introduced to reduce thermal conductivity, they also in turn reduce the carrier mobility within the material as it causes scattering among the charge carriers. As a result,

decreasing the thermal conductivity, can also decrease the carrier mobility and as a result, affect the overall ZT of the material [40]. However, there still are experimental ways to increase the overall ratio of thermal conductivity to the carrier mobility.

2.1.3 Improving Seebeck Coefficient

Considering the expression for ZT, it scales with S^2 and as a result of that, improving the Seebeck coefficient is more important than working on improving the electrical conductivity or decreasing the thermal conductivity. For an average semiconductor that has a parabolic band dispersion, and assuming the dopant has had no effect on the band structure or the scattering, the expression for Seebeck coefficient can be represented as follows:

$$S = \frac{8\pi^2 k_B^2}{3e\hbar^2} m_d^* T \left(\frac{\pi}{3n}\right)^{\frac{2}{3}}$$

In the above expression, m_d^*, k_B, e, and $\hbar$, represent total DOS (density of states) effective mass, Boltzmann constant, carrier charge and Planck constant, respectively.

2.1.4 Composite Formation

Composites is yet another route that can prove to be highly efficient when it comes to TE materials as it can enhance the TE properties of materials drastically. In layered structures, composites can settle in, in the form of sheets and can help in charge mobility or electron transport and that in turn can improve the overall ZT of the subject material. These can exist in the form of nanocomposites as well as in bulk form. Choosing the right composition is critical in forming a composite and achieving experimental perfection against the theoretical knowledge is also difficult to achieve, and as a result, the improvement shown cannot be drastic [29].

2.2 Bulk Thermoelectric Materials

Based on the optimum operating temperature range, TE materials are divided into 3 ranges which are as follows:

- **i.** TE materials with operating temperatures below 400K or low-temperature TE materials. These include $Bi_2Te_{3-y}Se_y$, $Mg_2Sn_{1-x}Ge_x$, $CsBi_4Te_6$, etc. [52-56].
- **ii.** TE materials with operating temperatures between 600K and 900K or medium-temperature TE materials. These include SnSe, MgAgSb, BiCuSeO, $CoSb_3$, etc. [57-64].
- **iii.** TE materials with operating temperatures beyond 900K or high-temperature TE materials. These include $Cu_{2-x}Se$, FeNbSb, etc. [65-67].

Since the discovery of the phenomena by Seebeck in 1821, TE materials have been through 3 generations with constant improvements. These generations and the improvement in ZT over time, can be seen in Figure 2.1. During the first period, the maximum value for ZT achieved was ~1.0 with a conversion efficiency of ~4%-5% as illustrated in the left section of Figure 2.1 [51]. The second period which is shown in the middle section of Figure 2.1 was fueled by the size effects and as a result, the ZT nearly doubled during that period, reaching the values of between 1.3 and 1.7 with an conversion efficiency ranging between 11-15%. This was achieved through nano-structuring and introduction of nano-scaled precipitates [51]. The third generation at the right end in the Figure 2.1 is still undergoing development and a new combination of materials for TE applications was introduced during this period which are the SnSe-based TE materials. The ZT value for this generation of TE materials ranges between 1.8 and 2.2, depending on the ΔT or the temperature difference, and the conversion efficiency range is approximately 15-20% [51]. This improvement is the result of multiple cutting-edge approaches to enhance the ZT which include but are not limited to; improving the Seebeck coefficient through enhanced carrier mobility, conduction band convergence, and reducing the lattice thermal conductivity [51].

As it can be seen from Figure 2.1, SnSe has achieved a relatively higher value of ZT and therefore, researchers have started to focus on SnSe-based TE materials as it has shown the potential of introducing TE materials for various applications. Although PbTe-based TE materials have also shown the potential to show drastic improvement but considering Pb is not environment-friendly and can be hazardous, the acceptance has not been wide and with the new ESG policies, the focus now is towards environment-friendly materials.

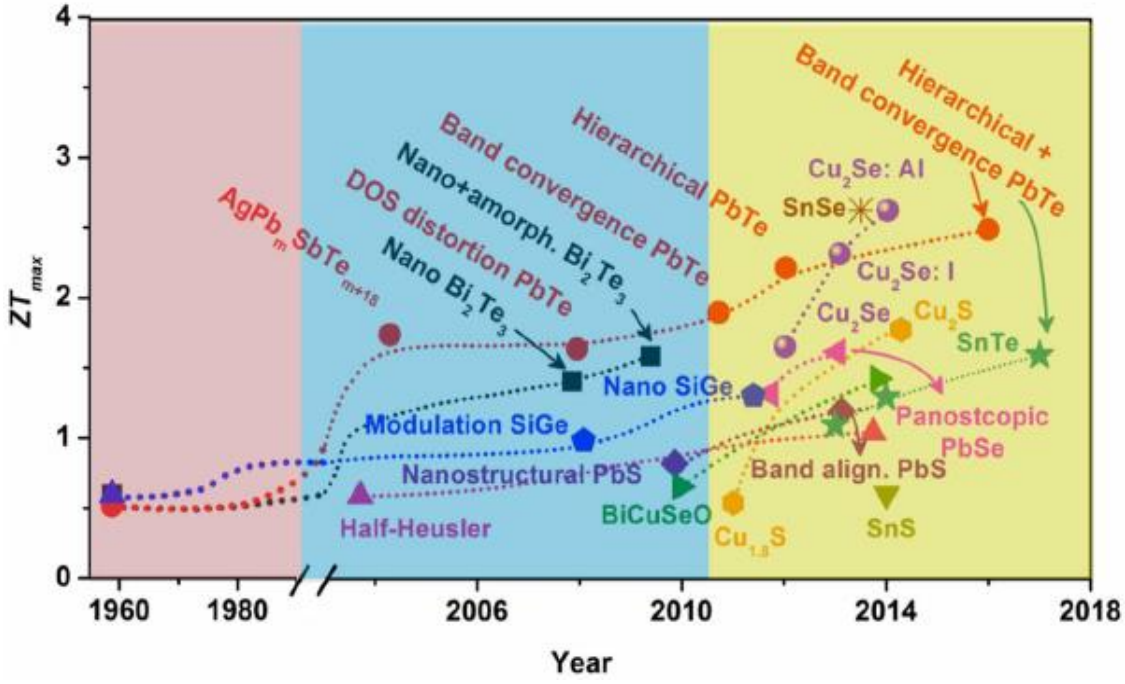

Figure 2.1 Evolution of TE materials during the three generations [51]

2.3 SnSe-based TE Materials

Tin selenide (SnSe) is a highly stable compound with simple structure and is also composes of earth-abundant materials and all these characteristics, make it a favorable TE candidate. Historically, as evident from Figure 2.1 also, SnSe-based TE materials did not get much attention and were never explored for TE applications. Later, due to its anisotropic and layered crystal structure, it became an encouraging candidate for TE applications, as its carrier transport properties were studied in all the axial directions.

2.3.1 SnSe Structure

The structure of SnSe is highly disfigured having a polyhedral coordination of Sn through three short bonds while there are 4 long Sn-Se bonds as well. The three short bonds are stronger than the long bonds and are attached to the nearest atom in the same bilayer. The remaining four bonds exist among two bilayers, in a way where two of the four bonds lie in same bilayer while the remaining two bonds lie in the next one. This leads to lattice anharmonicity, a phonon-scattering mechanism, in the SnSe-based compounds [79].

2.3.1.1 Anharmonic Bonding

Anharmonicity is a characteristic of lattice vibrations and it affects the heat transport in the SnSe structure. Sn and Se have anharmonic bonding in between the atoms of the crystal structure and this is the key reason why SnSe has ultralow thermal conductivity [79]. Figure 2.2 shows the relation between anharmonicity and harmonicity where a_0, r and $\Phi(r)$ represent lattice parameter, distance between the adjacent atoms and potential energy, respectively. Harmonicity displays a stabilized phonon transport.

In harmonicity, during the phonon transport, if an atom is bound to diverge from its stable or equilibrium position, the force applied is directly related to the displacement of displaced atom and this relationship is termed as stiffness or the spring constant [79]. On the contrary, in anharmonicity, the force applied is not proportional to the atom's displacement. As a result, in anharmonicity, the phonon transport is imbalanced which leads to improved phonon scattering and in conclusion, reduced the lattice thermal conductivity [80]. It should be known that in actual materials, the bonds are always anharmonic but the extent of anharmonicity keeps on changing [81].

2.3.1.2 Phonon Scattering Effect

As discussed in the previous section, the ultralow thermal conductivity of SnSe is the resultant of the strong anharmonic bonding and the layered crystal structure [82]. Having said that, phonon scattering can be a result of other reasons as well like lattice defects, for

instance, dislocations and point defects, and at the grain boundaries as well. Phonon scattering shows more prominence in polycrystalline structures. This phenomenon has been used as a noticeable tool to further strengthen the phonon scattering during charge transportation and as a result, reduce the overall lattice thermal conductivity [83]. Grain boundary scatterings have the capacity to introduce high levels of strain fields which result in higher phonon scatterings [84].

2.3.2 Mechanical Properties

Overall, mechanical properties of SnSe, including bending strength, fracture strength, fracture toughness, hardness, thermal shock resistance, and compressive strength, exhibit values that can be compared to other competing TE materials. The bending strength and the compressive strength of the polycrystalline SnSe were found out to be 40.6 MPa and 74.7 MPa, respectively [85]. SnSe is brittle in nature and that's why, the hardness value obtained through Vickers indentation test was 0.27 under a load of 0.98 N and a time of 10 seconds. These values are comparable to other TE materials like Bi_2Te_3 and PbTe [86].

2.4 $SnSe_2$ Structural Characteristics

Tin diselenide ($SnSe_2$) is an inorganic semiconductor compound and its molar mass is 276.63g/mol. In comparison to SnSe, $SnSe_2$ has a lower melting point at 650 °C [68]. The structural characteristics of $SnSe_2$ will be studied in this section in detail.

2.4.1 Generic Structure

$SnSe_2$ is a member of layered semiconductors' family and can be generally represented as MX_2, where M represents a metal and X represents a chalcogen. [70-72]. $SnSe_2$ possesses distinctive chemical and physical properties due to its layered structure and as a result, it offers a broad area of opportunities where it can be utilized as an electrode material in lithium-ion battery packs, electric keys, memory elements, hetero-structures of SnS_2-$SnSe_2$-SnS_2 that are created as a result of van der Waals epitaxy [69]. Studying the electronic structure of $SnSe_2$ is of prime importance as it can help us in deriving its

physical properties and as a result, the field of electronic devices can then be enriched with SnSe-based devices.

2.4.2 Electronic Structure

Numerous studies have been carried out to analyze the electronic structure of $SnSe_2$ in its simplest form as 2H-polytype. Multiple calculation methods have been used like local empirical pseudopotential method, empirical pseudopotential method, tight binding method, priori pseudopotential method, etc. [73-78]. Although, through these methods, qualitative reproducibility of the important features of the electronic structure of 2H-polytype $SnSe_2$ was achieved, but quantitative reproducibility could not be achieved. There existed differences in values of band gaps, both direct and indirect; overall breadth of valence bands; characteristics of the density of states; topology and sequence of the energy bands; and most importantly, localization of the conduction band bottom and valence band top, consequently, differences in indirect and direct band gaps. As a result, it becomes difficult to compare the results.

2.4.3 Crystal Structure

Polytype 2H-$SnSe_2$ is a three-layered structure and is characterized by brucite type structure due to this reason. The layers exist in the form of sandwiches and the formation adopted is -Se-Sn-Se- packets. These layers lie parallel to the (001) plane. The three-layer sandwich consists of 2 monolayered selenium (Se) atoms which enclose a monolayer of tin (Sn) atoms. The spacing between the atomic monolayers within a sandwich, comes in at 1.53 Å while that between the sandwiches is almost double, coming in at 3.08 Å. The 2H-$SnSe_2$, in its crystal structure, has Sn atoms that are centered in the octahedrons while Se atoms are placed at the vertices. The octahedra are attached to each other on the common edges, forming the three-layered packets. The bonding among the layers is van der Waals forces while that between the packets is covalent and as a result, wider array of anisotropy when it comes to the physical properties [69]. $SnSe_2$ is a layered chalcogenide structure with the tunability of electronic transport properties like electrical conductivity and Seebeck, via careful control of the number of layers and morphology. Therefore,

$SnSe_2$ and other similar compounds are expected to perform better as a thermoelectric material, if its thermal and electronic transport properties are properly engineered.

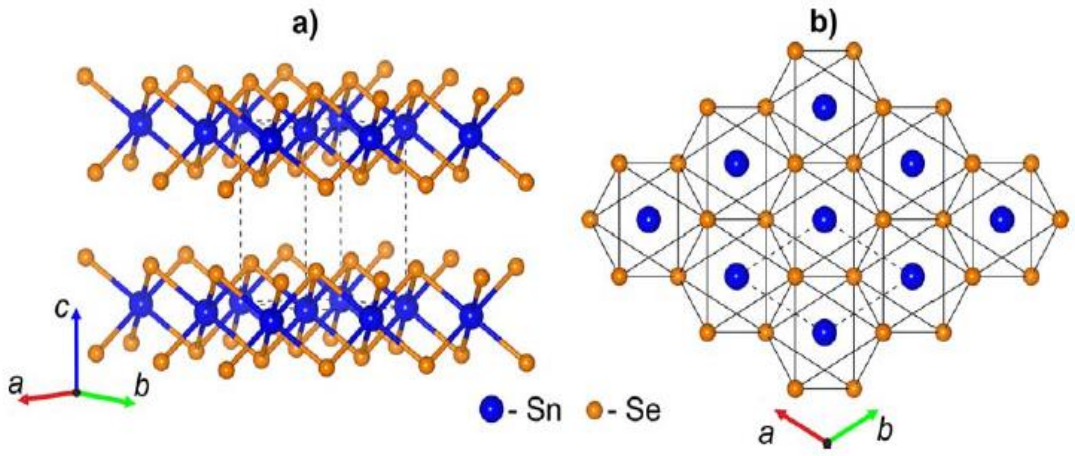

Figure 2.2 (a) 3D Crystal Structure of $SnSe_2$ and **(b)** Crystal Structure of $SnSe_2$ on XY plane [69]

2.5 Characteristics of GO

Because of its unique 2D structure, graphene has excellent thermal and electrical properties. At standard room temperature, the carrier mobility, thermal conductivity, electrical conductivity and carrier mobility of graphene are $5x10^3$ $W.m^{-1}.K^{-1}$, $1x10^6$ S/m, and $2x10^5$ $cm^2.V^{-1}.s^{-1}$, respectively. Meanwhile, the graphene carrier with 0 bandgap can switch between electron and hold continuously, and that can aid with electronic transport and can enhance the electrical conductivity as a result of that. This characteristic of graphene oxide helps at the p–n interfacial region in prominence.

In order to generate GO, exfoliation of graphite oxide can be performed with any organic solvent, resulting in multiple forms of exfoliated layers with varying single-layer thickness and the stability of the structure as well. NMP, THF, DMF, and ethylene glycol are among the kinds of organic solvents that are or can be used to obtain a single exfoliated

layer of GO sheet, just like water [88]. Electrical conductivity of GO can be increased once the oxygen functional group is removed [91].

CHAPTER 3 EXPERIMENTAL WORK

3.1 Material Selection

3.1.1 GO

- Graphite Powder
- Phosphoric Acid (H_3PO_4)
- Sulfuric Acid (H_2SO_4)
- Potassium Permanganate ($KMnO_4$)
- Hydrogen Peroxide (H_2O_2)
- Ethanol (C_2H_6O)

3.1.2 $SnSe_2$-rGO

- Tin Chloride ($SnCl_2.2H_2O$)
- Selenium dioxide (SeO_2)
- Polyvinylpyrrolidone (PVP)
- Benzyl Alcohol ($C_6H_5CH_2OH$)
- Ethanol (C_2H_6O)
- Graphene Oxide (GO)

3.2 Synthesis of GO

Graphene oxide (GO) was synthesized using pure graphite powder through modified hummers method in a conventional procedure. In this approach, sulfuric acid (H_2SO_4) and phosphoric acid (H_3PO_4) in the amount of 27ml and 3ml, respectively, were mixed and agitated for many minutes (volume ratio 9:1). This gave a pale-colored solution. Then, while stirring, graphite powder was added to the mixed solution in the amount of 0.225g. After that, 1.32g of potassium permanganate ($KMnO_4$) was progressively added to the solution. The solution was swirled for 6 hours till it turned dark green. 0.675ml hydrogen

peroxide (H_2O_2) was added progressively and agitated for 10 minutes to remove excess $KMnO_4$. The exothermic reaction took place, and it was allowed to then cool down. Ethanol (C_2H_6O) was then added to the resultant solution and was mixed. Then the solution was centrifuged at 4500rpm until the powder settled at the bottom. After that, the excess liquid was drained and ethanol was added again to the settled powder and mixed together in order to wash off the contaminants. Once it became a suspension, it was again centrifuged at 4500rpm for 10 minutes. This process was repeated 3 times when clear water-like liquid was obtained.

In order to obtain the desired GO powder, the excess ethanol was drained with a concentrated suspension left at the bottom. This suspension was then placed in an oven at 90°C for 24 hours until the ethanol was completely dried. The powder that remained at the bottom was collected and stored safely for the next experiments.

The schematic diagram of the process can be seen in Figure 3.1 and the experimentation schematic can be seen in Figure 3.2.

3.3 Synthesis of $SnSe_2$

For synthesizing $SnSe_2$, 40ml Benzyl Alcohol which was used as a solvent, was poured in a beaker that was put on hot plate at room temperature. 6g PVP was added to the beaker. PVP acts as a growth modifier, surface stabilizer and as a reducing agent. After the addition of PVP magnetic stirring was started. The stirring was allowed to go on for 10 mins and as a result PVP was dissolved in Benzyl Alcohol and a clear liquid was obtained. Once a clear solution was obtained, 1.32g of $SnCl_2.2H_2O$ was added to the solution as the first reactant. The magnetic stirring continued for 15 minutes and as a result, a light yellowish solution was obtained after the complete dissolving of the first reactant.

Once the first reactant was dissolved, SeO_2 was added as the second reactant. The amount by weight was 0.9g. After the addition, the solution quickly turned into light orange colored solution. The magnetic stirring continued for 30 minutes and as a result, a dark orange solution was obtained. This solution was then put in autoclave, in an exothermic

reactor for heat treatment at 180°C. The solution was left in the reactor for 16 hours and was then retrieved on the next day in a falcon tube.

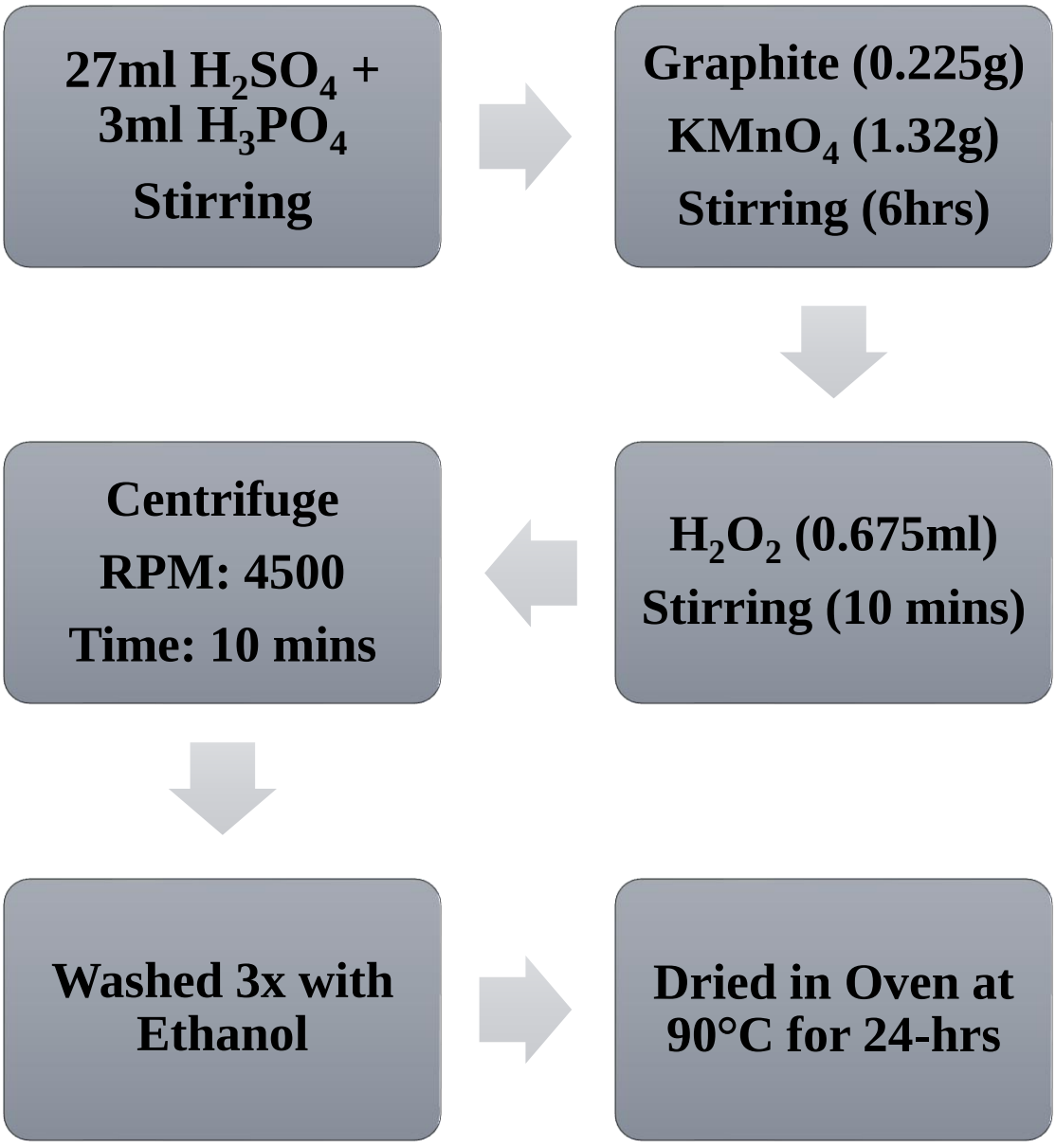

Figure 3.1 Schematic Diagram of Modified Hummers Method for GO Synthesis

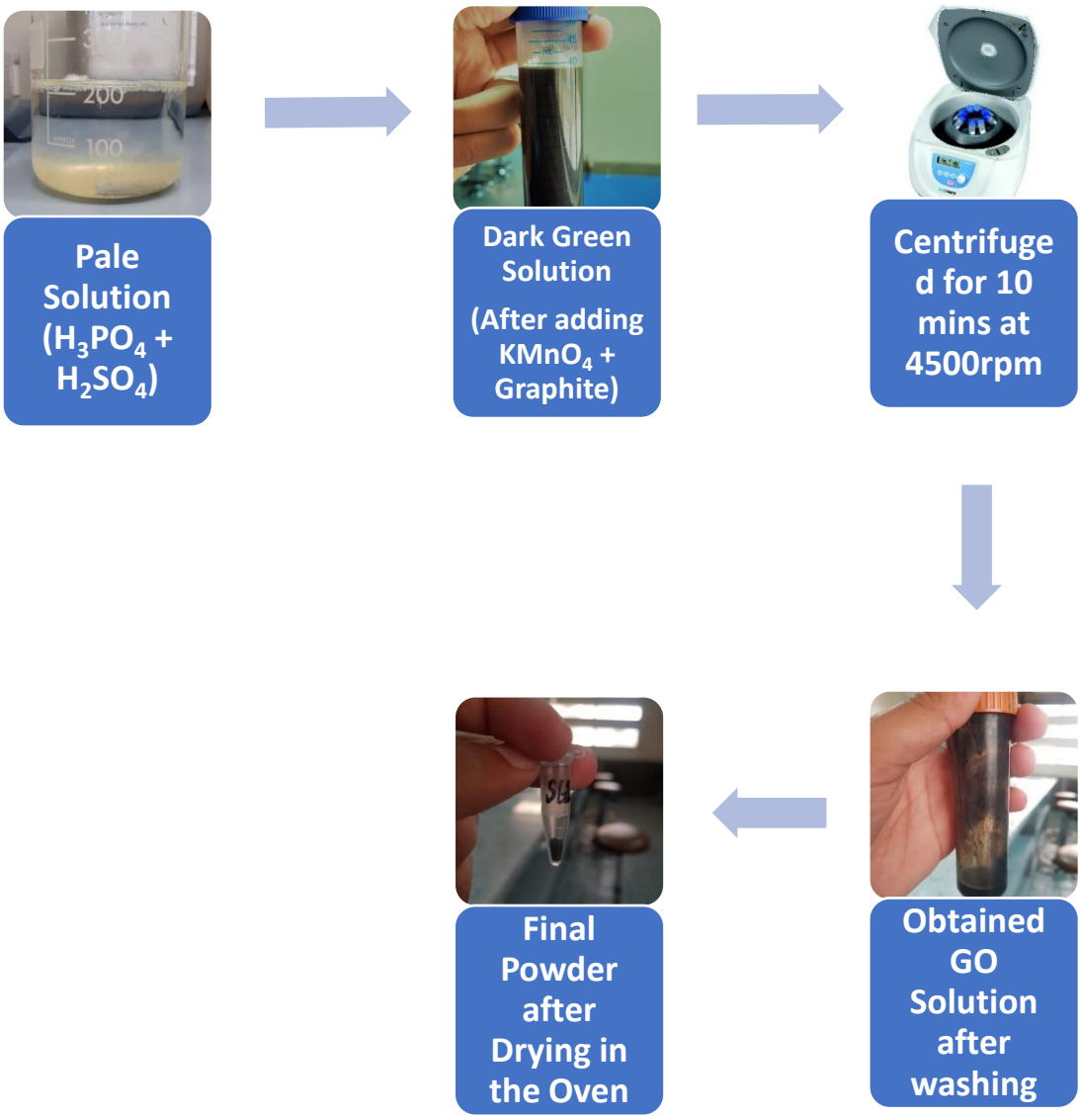

Figure 3.2 Experimental Design of GO Synthesis

The obtained solution was then centrifuged at 4500rpm for 30 minutes until a black powder settled at the bottom. The excess liquid was drained and ethanol was added to the settled black powder and the powder was again mixed in ethanol and put in the centrifuge under same conditions. This process was repeated 3 times and as a result, clear ethanol was obtained. The excess ethanol was drained and the remaining black powder with traces of ethanol was dried in an oven at 90°C for 24 hours. As a result, a black powder was obtained, which was stored for further experimentation.

The schematic diagram is shown in Figure 3.3 and the experimental design can be seen in Figure 3.4.

3.4 Synthesis of $SnSe_2$-GO Composite

For synthesizing $SnSe_2$-GO composite, the same methodology was used as the one explained in Section 3.3. The process involved starting with Benzyl Alcohol (40ml), then addition of PVP (6g) and then the beaker was placed on a hot plate at room temperature. Once the PVP was dissolved, 1.32g of $SnCl_2.2H_2O$ was added to the solution and stirred for 15 minutes. After that, SeO_2 was added and the stirring continued for 30 more minutes. A dark orange solution was obtained. Once dark orange solution was obtained, the GO powder obtained from experiment explained in Section 3.2 was used in 3 different amounts by weight. For the first experiment, the amount used was 0.01g or 0.4%, for second experiment, the amount was 0.125g or 5.7% and for the third experiment, the amount was 0.25g or 11.7%. The stirring continued after that for 10 more minutes.

After that, the obtained solution was transferred to an Autoclave and was put in an exothermic reactor at 180°C for 16 hours. After that, the solution was put in a falcon tube and centrifuged at 4500rpm for 30 minutes. The powder settled at the bottom as a result of that. Excess liquid was drained and the powder was then washed with ethanol thrice and centrifuged every time for 30 minutes at 4500rpm. Finally, $SnSe_2$-GO powder was obtained with traces of ethanol which was dried in an oven at 90°C for 24 hours and the dried powder was then stored for proceeding experimentation.

The schematic diagram can be seen in Figure 3.5.

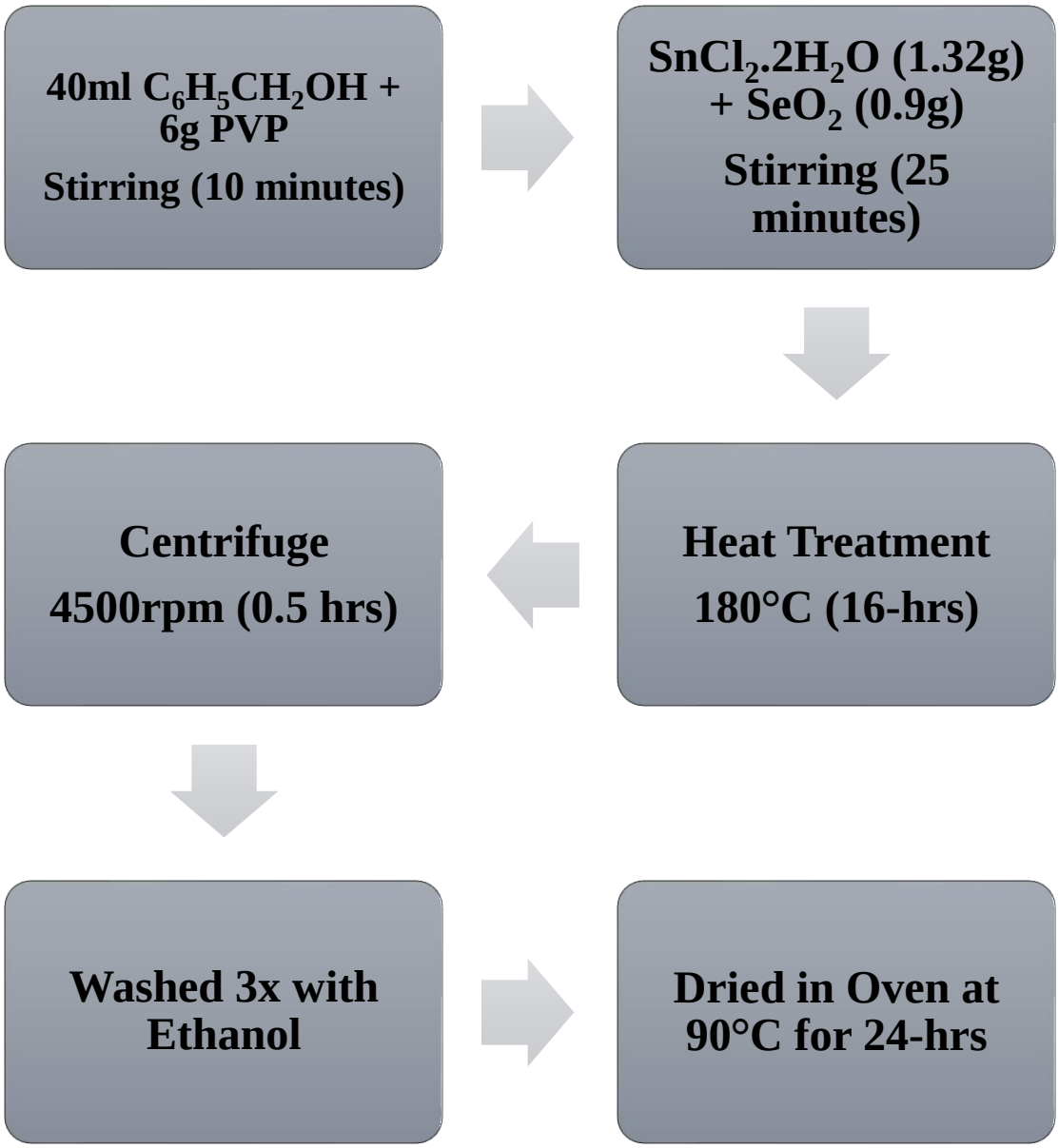

Figure 3.3 Schematic Diagram of $SnSe_2$ Synthesis

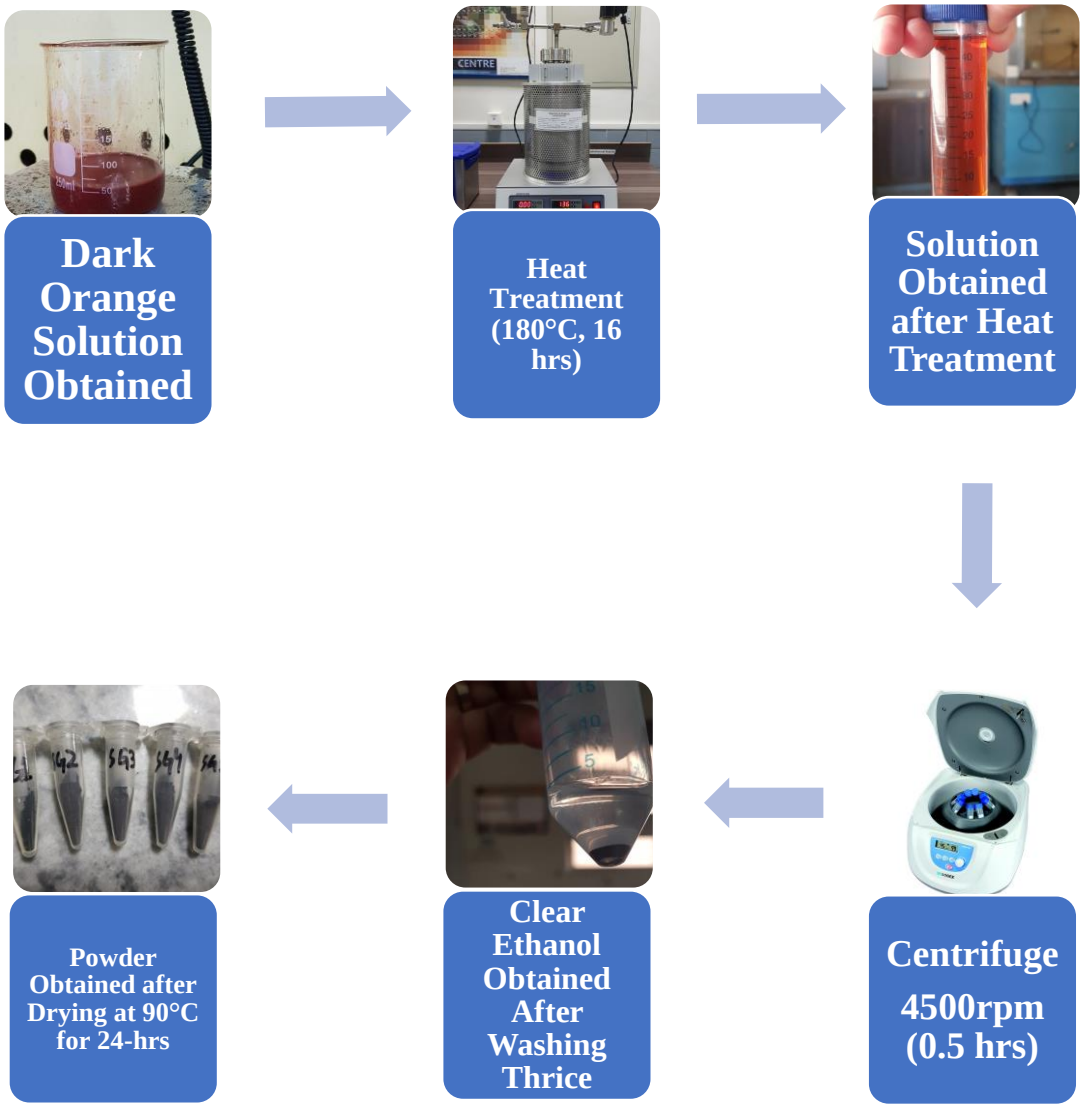

Figure 3.4 Experimental Design of $SnSe_2$ Synthesis

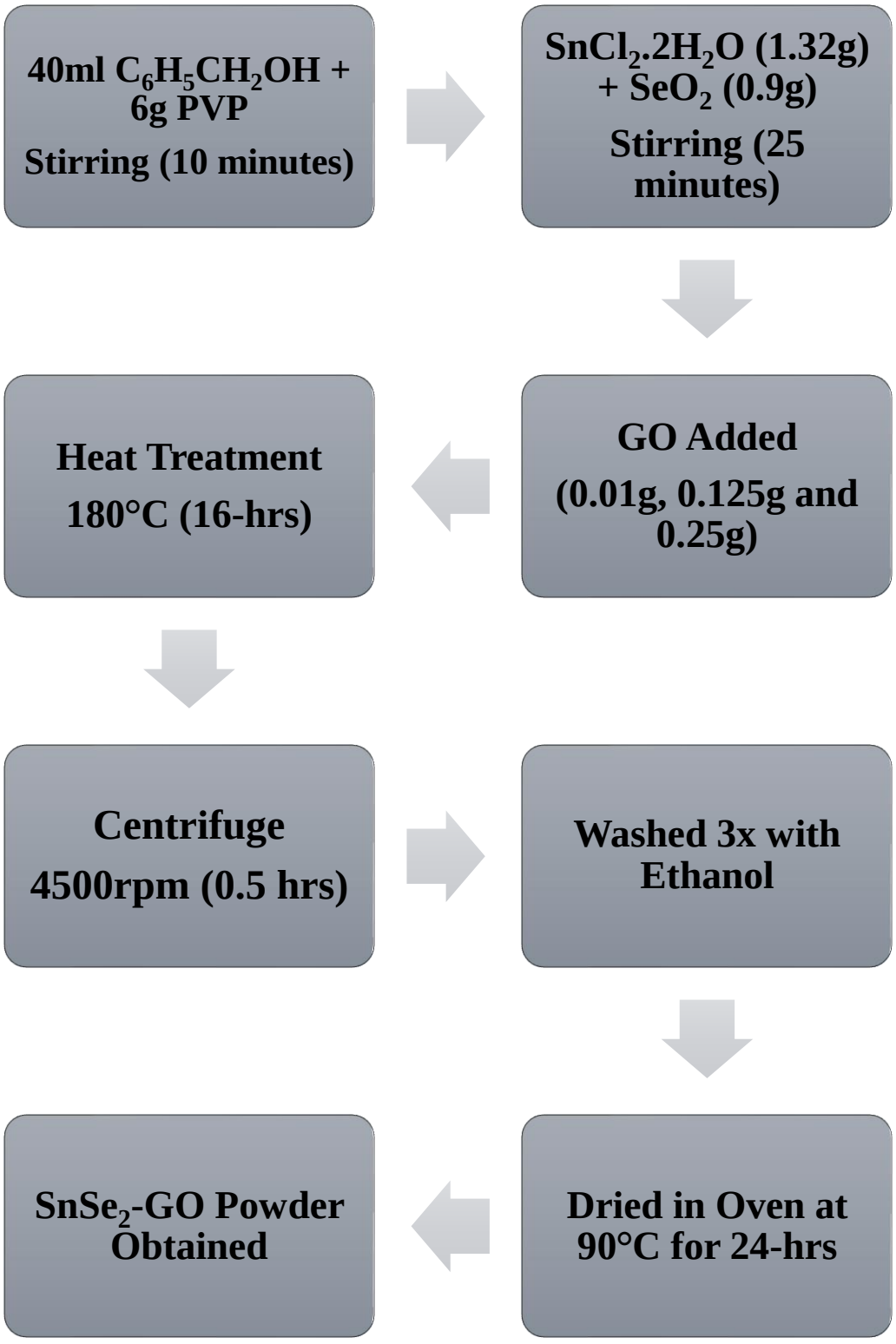

Figure 3.5 Schematic diagram of $SnSe_2$-GO Synthesis

3.5 Synthesis of $SnSe_2$-rGO Composite

After the powders of GO, $SnSe_2$ and $SnSe_2$-GO were obtained from the experimental work, these powder specimens were processed for pellet formation. For this purpose, a custom die was designed, with a diameter of 8mm and it was used to make pellets in a hydraulic press. The die was manufactured by a fabrication specialist on a lathe machine, under supervision. Once the die was created, it was thoroughly cleaned using ethanol to remove all the contaminants, if any. After cleaning the die, it was filled with $SnSe_2$ powder and the die was placed in a hydraulic press. The sample was pressed in the hydraulic press under a pressure of 7.5psi for 15 seconds. After that, the die was released and a solid pellet was retrieved. The first pellet that was made from pure $SnSe_2$ powder was the first sample, named 1-S.

After that, the die was thoroughly cleaned again, with ethanol and this time, $SnSe_2$-GO powder with 0.4% GO concentration was used in the die to obtain another pellet which was the second sample and was named, 2-SG. The die was cleaned with ethanol and the process was repeated again for $SnSe_2$-GO with 5.7% GO concentration and $SnSe_2$-GO with 11.7% GO concentration, in order to obtain the remaining 2 samples namely, 3-SG and 4-SG, respectively.

Once the pellet samples, 1-S, 2-SG, 3-SG and 4-SG were obtained using custom die and hydraulic press, these samples were then sintered. For sintering, Protherm Tube Furnace was used. In order to start the process, all the samples were placed in a ceramic boat at a distance from each other. The ceramic boat was then wrapped in an aluminum foil and small holes were made in the file to allow volatile gases to escape in order to avoid contamination. After that, the foil-covered ceramic boat was placed in a transparent quartz tube which was 12 inches in length. The tube was sealed from both the sides and an inlet was provided for introduction of Argon gas in order to provide an inert media for the sintering.

The packed quartz tube was placed in the tube furnace and the temperature was set to 550°C and sintering was performed for 4-hrs at 550°C. The step increment used was 5°C rise in temperature per minute. The sintering helped in reduction of GO to form rGO, resulting in $SnSe_2$-rGO composite. Once the samples were sintered at 550°C for 4-hrs, the

samples were allowed to cool down in normalizing way. Once the samples reached the room temperature, they were removed from the furnace and stored in separate tubes to avoid contact and contamination and for further process of analysis.

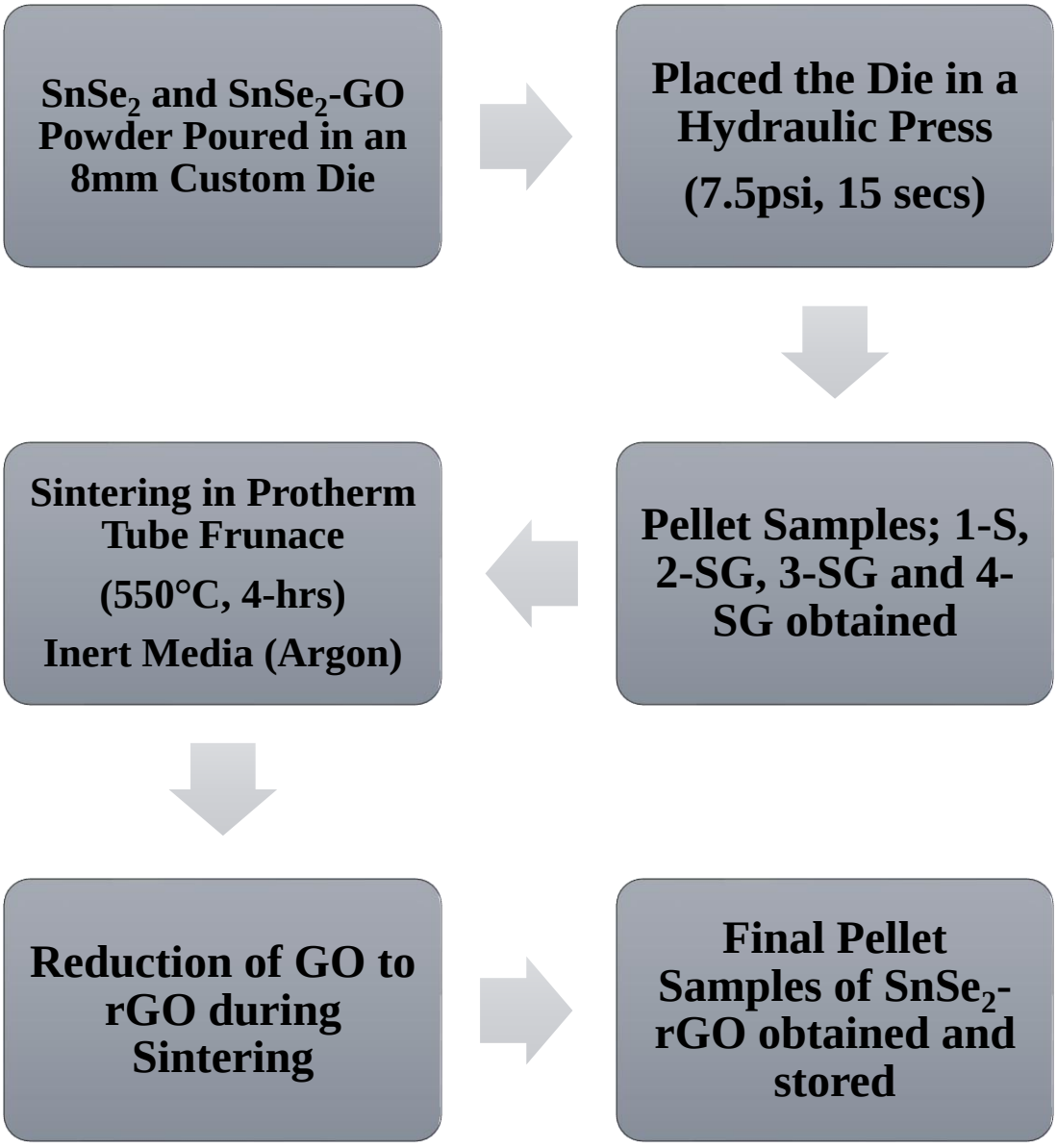

Figure 3.6 Schematic Diagram of $SnSe_2$-rGO Composite Synthesis

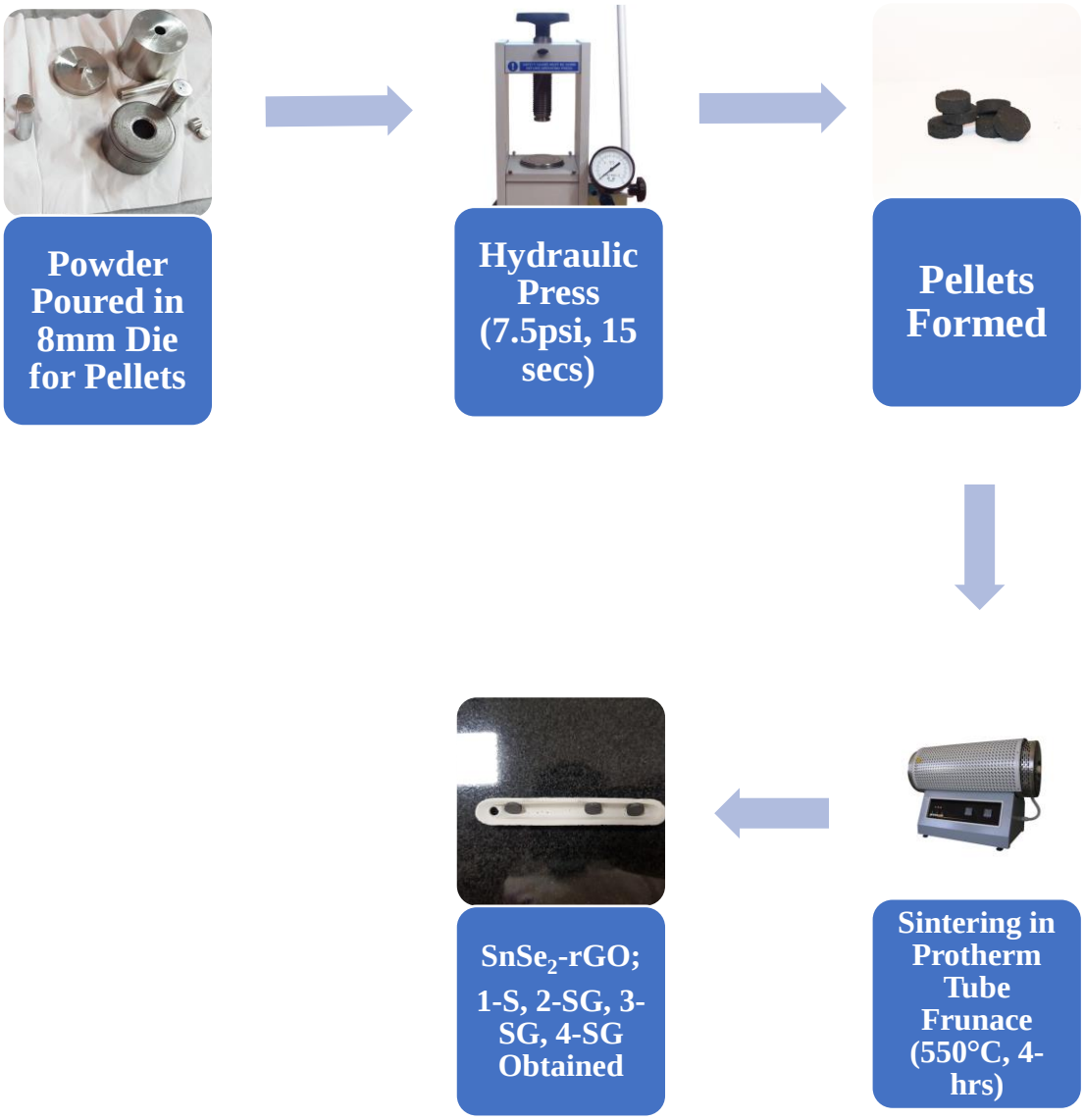

Figure 3.7 Experimental Design of $SnSe_2$-rGO Composite Synthesis

The schematic diagram can be seen in Figure 3.6 and experimental design can be seen in Figure 3.7.

3.6 Characterization Techniques

There are multiple techniques that can be used for characterization of $SnSe_2$ and $SnSe_2$-rGO pellets but in accordance to the required results, we chose the following techniques:

- XRD
- SEM
- UV-Visible Spectrophotometry
- Hall Measurement
- Laser Flash Analysis
- Thermoelectric Characterization Apparatus

3.6.1 X-ray Diffraction (XRD)

X-ray diffractometer or XRD is used to investigate crystal structure as well as identify the various elements and compounds that are present in a sample under observation. The technique involves striking X-rays on the outer surface of a sample material. The incident X-rays follow a certain angle of incidence. The incident rays are then diffracted after striking the crystal lattice and interfere with each other in negative or positive way. As a next step to that, constructive interference gives us the information about the crystal structure. This information can include atom kinds, atomic arrangement, atomic positioning, interatomic distances, etc. This interference is actually based on Bragg's Law. In essence, Bragg's Law asserts that X-rays, that have a path difference that is equal to an integral multiple of wavelength, will encounter constructive interference, given that following conditions are fulfilled:

$$\mathbf{n\lambda = 2dsin\theta}$$

where n represents order of diffraction, λ is the wavelength, d means interplanar spacing, and θ represents incident wave angle. The incident and reflected X-rays from a crystal lattice, while satisfying Bragg's law, are shown in Figure 3.8.

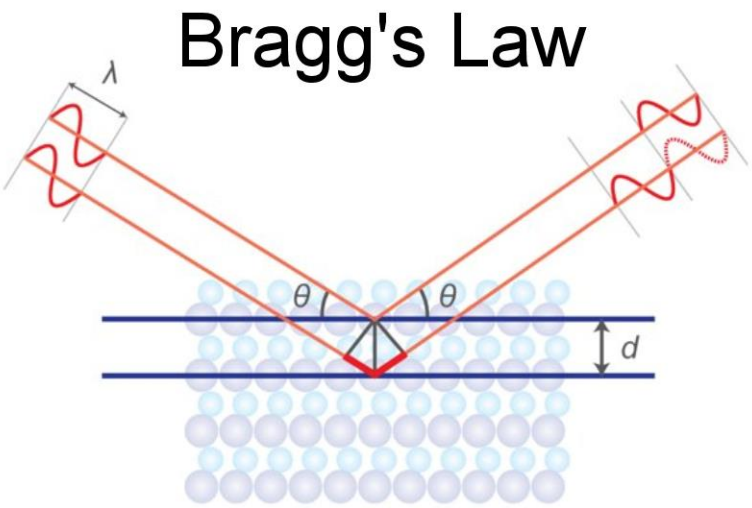

Figure 3.8 X-ray Diffraction and Bragg's Law Interpretation [98]

After X-ray diffraction, the intensity versus angle or 2θ plot is obtained which shows the distinct peaks for crystalline sample materials while hump for amorphous sample materials. The positioning of the peak is dependent on the Interatomic distances while the positioning and kind of atom determines the strength of the peaks. It should also be noted that the sharpness or gradual increase in the peak is also dependent on the subject material that is under observation. Also, the width of the diffracted peak is dependent on the microstructure of the sample material. Once the results are obtained, the XRD patterns can be confirmed by comparing them to a reference card that is deemed as standard. A software can also be used for doing this. One famous software is X'pert HighScore Plus.

3.6.2 Scanning Electron Microscope (SEM)

Scanning Electron Microscope or SEM is a very valuable characterization tool in the world of Material Science and Engineering. It is used for determining morphology, size, chemical content, microstructure, surface topography, form and phase differences. The operation phenomenon includes condenser and objective lenses which concentrate and converge an electron beam that is generated by a hot filament source or an electron gun,

onto the outer surface of the subject sample. This electron beam then interacts with the surface of the sample. This interaction can be both elastic or inelastic, however, both interactions are desired.

Figure 3.9 Scanning Electron Microscope (SEM) [99]

As stated, elastic interaction is the desired interaction as it produces the back-scattered electrons and this set of electrons is responsible for providing the required information about the subject sample. This information includes but is not limited to, compositional

variation, as the darkness or the brightness of the phases depend upon the lower or higher atomic numbers, respectively. As a result of inelastic interactions, secondary electrons come into existence and these electrons provide the desired information about the topography or the outer surface of the subject sample. These electron-based signals are detected and then are amplified by the available amplifier. SEM has the capacity to help us observe a sample of the size of 1 cm to 5 microns and the magnification can be in the range of 20X to 30,000X.

To examine our sample, we employed a Scanning Electron Microscope (SEM, Model JEOL JSM-64900). Figure 3.9 shows a working model of SEM.

3.6.3 UV-Visible Spectrophotometry

UV-visible spectrophotometry or UV-Vis is a technique that is used for determining the light that is absorbed in the visible and ultraviolet wavelength ranges of the electromagnetic spectrum. Incident light can be reflected, transmitted or absorbed when it strikes materials. When the UV-Vis radiations are absorbed by the subject material, it leads to atomic excitation which then results in molecules moving from low-energy state to higher energy state or excited state.

For an atom to change its excitation state, it is important that it should absorb sufficient amount of radiation, so that the electrons can move towards higher-energy molecular orbits. If a sample material absorbs light of shorter wavelength, it means that it has a shorter bandgap and vice versa. As can be interpreted from the previous statement, the required energy for molecules to make this transition is electrochemically very specific. UV-Vis uses this approach to quantify test samples depending upon their absorption quality. The data obtained from this technique can be used for both quantitative analysis as well as qualitative analysis of a subject material.

Figure 3.10 UV-Visible Spectrophotometer [95]

During the process of analysis, it is absolutely critical to use a reference cuvette which contains the solvent liquid, in order to calibrate the equipment. Once the equipment is calibrated, solvent along with sample, in the form of solution, can be placed in the equipment to study the absorption. In this case, the solvent liquid used was Ethanol. Figure 3.11 shows the model of a UV-Visible Spectrophotometer.

3.6.4 Hall Effect Measurement System

Hall effect is governed by Lorentz Force which is one of the fundamental principles of Physics. When the movement of an electron is perpendicular to the magnetic field, an encountering force is experienced by this electron which is normal to both the directions and moves against this force along with electric field's force within. The Lorentz Force can be calculated using the following equation:

$$\underline{F}_{Lorentz} = q[\underline{E} + (\underline{v} \times \underline{B})]$$

where,

$F_{Lorentz}$ = Lorentz Force

q = electric charge

E = external electric field

v = velocity

B = magnetic field

Hall Measurement Systems are basically used to determine carrier mobility, carrier concentration and semiconductor resistivity. The measurements obtained from Hall measurement system can be used for the characterization of both compound semiconductors as well as semiconductors.

A filter or a dryer, a vacuum chamber, a thermal stage, gas lines, refined high-pressure gas, magnet structure, spring loaded probes, a vacuum pump and a computer are all part of Hall Measurement System.

The process starts with a sample that is connected to a battery, completing a circuit. The current is allowed to flow through the circuit. As a result of the flowing current, the charge carrier flow from one end to the other, following a linear path. As a result of the movement of the charge carriers, a magnetic field is produced. There is a magnet placed near the sample and when the magnetic field produced due to charge carriers comes in contact with the magnetic field of the magnet placed near the sample, there is an interference and as a result, a distortion is produced. This distortion results in a force which is termed as Lorentz Force. This force distorts the charge carriers and interferes with their direction as well.

As a result of this interference, the electrons in the circuit start to flow towards one side while the holes start flowing towards the other.

Figure 3.11 Hall Effect Measurement System [96]

The potential difference created as a result of the movement of electrons and holes is termed as Hall Voltage and it is given by;

$$V_H = \frac{IB}{qnd}$$

where,

V_H = Hall voltage

I = current that flows through the circuit

B = magnetic field

q = charge in the circuit

n = no. of charge carriers

d = thickness

Figure 3.12 shows an image of Hall Effect Measurement System.

3.6.5 Laser Flash Analysis (LFA)

The Laser Flash or Light Flash method or LFA is used to determine the thermal diffusivity of different materials. A sample is placed in a tubelike structure, as shown in Figure 3.5 and one side of the sample is heated with a light pulse or laser flash. As a result, the temperature on the front face of the sample rises and the same rise, due to the law of diffusion, passes on to the rear front of the sample. This is noted by the infrared detectors present within the apparatus. It should be noted that the time it takes for the heat to reach the rear end is dependent on the diffusivity. Higher the diffusivity, lower will be the time taken by the heat to reach the rear end.

Thermal diffusivity is a property which varies from one material to another and it is used for characterization of unsteady conduction of heat in different materials. The value of thermal diffusivity determines how rapidly a material responds to a temperature change.

Thermal diffusivity is used to calculate the thermal conductivity of a sample material through the following mathematical expression:

$$\lambda = \alpha \times \rho \times C_{ps}$$

where,

λ = Thermal conductivity

α = Thermal diffusivity

ρ = Density

C_{ps} = Specific heat capacity

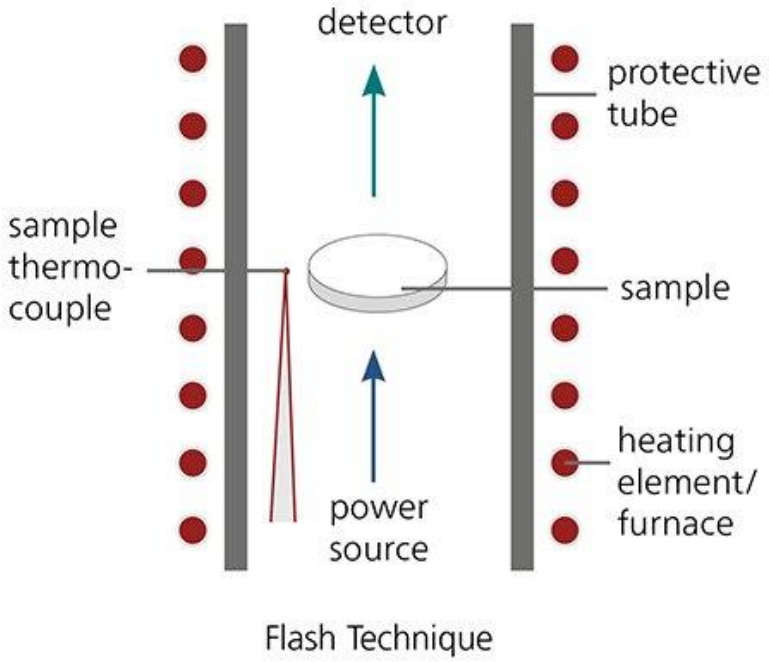

Figure 3.12 LFA Working Phenomenon [94]

Figure 3.13 NETZSCH LFA-457 MicroFlash [94]

For this research, NETZSCH LFA-457 MicroFlash (University of Oslo, Norway) was used. It can be used to measure thermal diffusivity and specific heat. This data is then used for calculating the thermal conductivity as is evident from the above expression.

Figure 3.13 displays the working phenomenon of LFA while Figure 3.14 shows an image of NETZSCH LFA-457 MicroFlash.

3.6.6 Thermoelectric Characterization Apparatus

A custom designed thermoelectric characterization apparatus was used for studying the TE properties of the samples. This apparatus was designed by researchers of University of Oslo, Norway and is now used as fully functional apparatus for TE research students. In this apparatus, a measurement cell exists in a tubular shaped vertical furnace that has a temperature controller as well. The sample is mounted in this cell and once it is mounted, the cell is sealed tightly in a quartz tube. It is then placed in the aforementioned tubular vertical furnace and chosen gas is used to flush into the furnace body to provide inert media. The pressure in this chamber is 1 atm. A total of 3 thermocouples (TCs), with thin wires (d=0.2mm), are used in the apparatus in order to act as both voltage and temperature probe. By doing so, no corrections are needed once the reading is taken and the values registered can be used as error-free final values [92].

These TCs are fixed in place using spring load mechanism. These springs are located at the lower end of the chamber in order to avoid exposure to high temperatures as it is optimum to keep them at room temperature. TC-1 is placed in close contact to the bottom of the sample, TC-2 is placed on the top of the sample while TC-3 is also on top but at a horizontal distance of 10mm from TC-2. Two Pt10Rh-coils are also used as a part of this apparatus, with 5 ohm as room temperature resistance and are located behind TC-2, next to TC-1, below the sample. Finally, 4 platinum wires are kept in contact with the sample and are held in place by the spring-load mechanism. These wires act as voltage and temperature probes and are used for measuring the resistivity which then leads to calculating electrical conductivity. This phenomenon is a practical representation of van der Pauw method [92].

This apparatus was used to determine the in-plane conductivity. The apparatus is suitable for disk and bar shaped samples. However, for bar shaped samples, 2 additional platinum wires are required. Figure 3.15 is a schematic representation of the TE Characterization Apparatus [92].

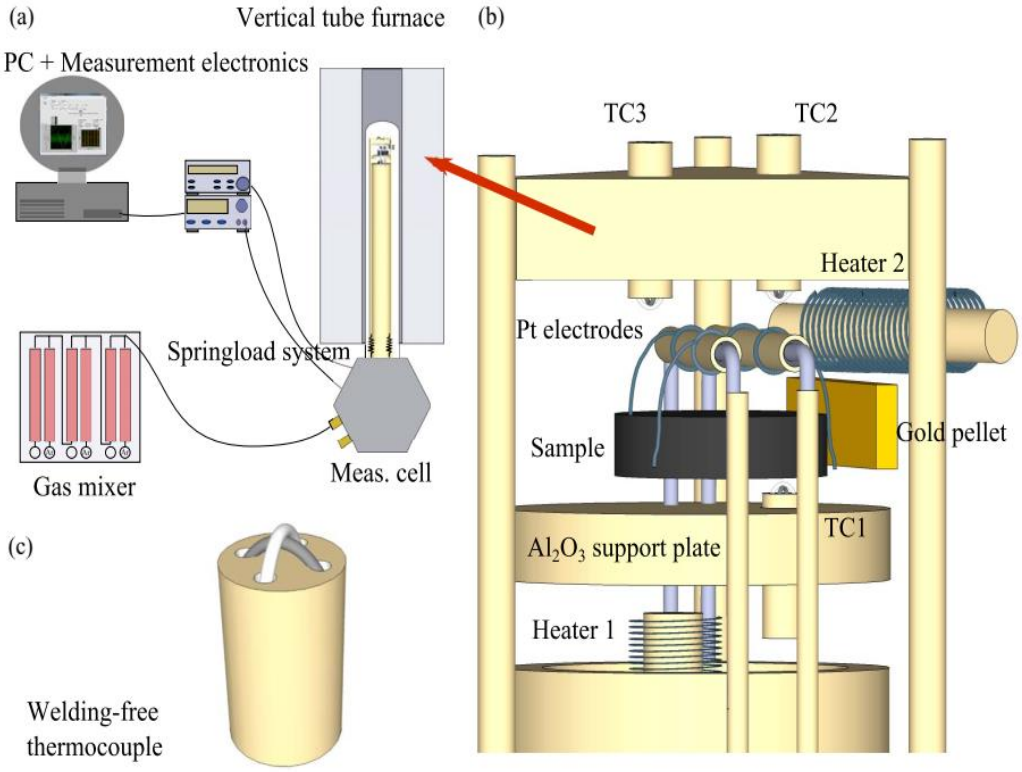

Figure 3.14 (a) Apparatus mounted inside the cell while connected to PC for measurement, **(b)** a close-up of sample (disk-shaped) placed in the heating area of the tubular furnace, and **(c)** a design of weld-free TC [92]

For Seebeck measurement, the same setup is used. This apparatus is capable of measuring Seebeck and Resistivity simultaneously. The phenomenon for determining the Seebeck revolves around the open-circuit voltage or ΔU that is created as a result of ΔT. For Seebeck, temperature is changed within a certain range and the change in voltage is recorded. The temperature is controlled by increasing the heating power of the heater that

is present inside as shown in Figure 3.15. Temperature and voltage of the TC's platinum leads are noted down using a voltmeter, one after the other. This creates thermal drift as a result and to avoid that erroneous result, the temperatures are measured both before as well as after the voltage is noted down. The Seebeck in essence, is measured from the applied voltage's slope versus the temperature difference that is induced by the operator [92].

CHAPTER 4 RESULTS AND DISCUSSION

4.1 Structural Analysis (XRD)

The structural analysis of the samples was performed using XRD technique. Figure 4.1 illustrates the resultant peaks of all the 5 samples that were obtained in order to identify the composition.

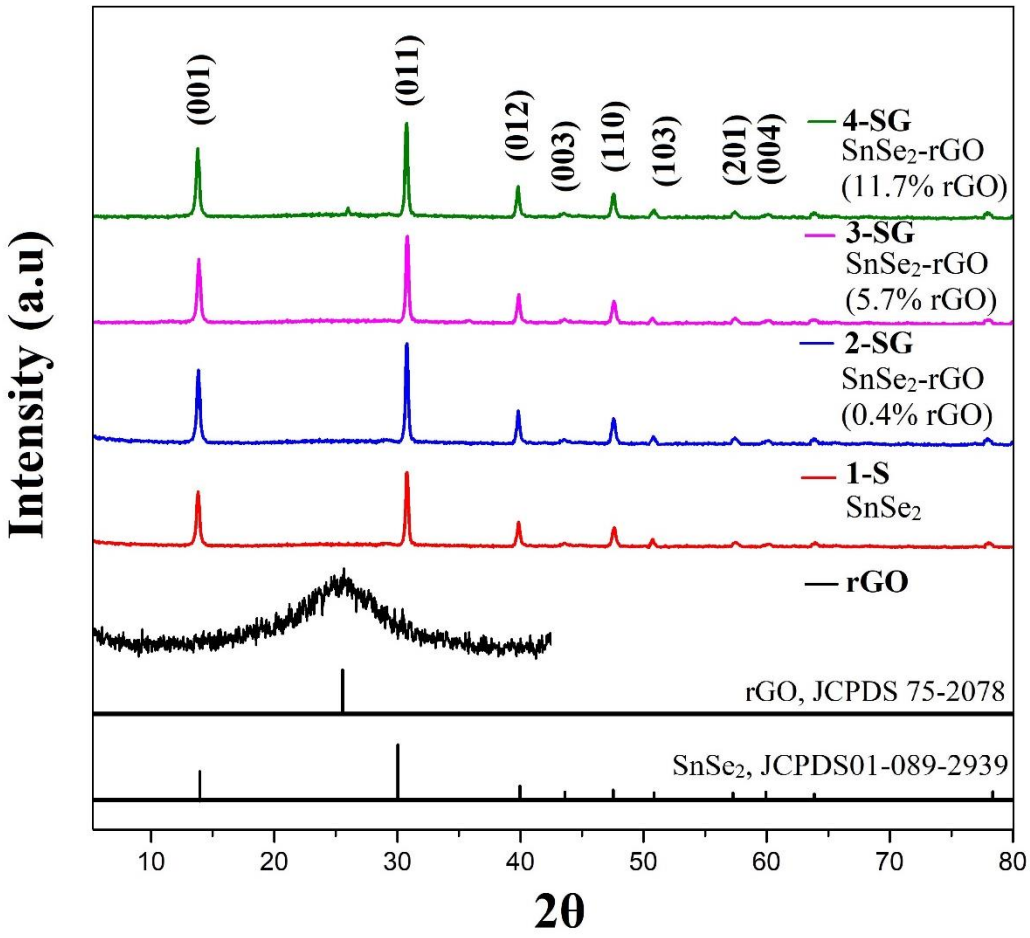

Figure 4.1 XRD Patterns of rGO, 1-S ($SnSe_2$), 2-SG (0.4% rGO), 3-SG (5.7% rGO) and 4-SG (11.7% rGO)

In Figure 4.1, starting from the bottom, we can see the characteristic (002) peak of rGO lies at 2θ=26°. The XRD analysis of rGO sample shows presence of graphene oxide in the sample which is the desired composition. It can also be confirmed with JCPDS 75-

2078. After the desired rGO was obtained, the further experimentation was resumed as it was the primary requirement in order to achieve the required composite. The XRD patterns for 1-S, pure $SnSe_2$, which can be seen represented by a red line, shows the peaks for pure $SnSe_2$. The patterns show narrow sharp peaks at 2θ angles of 14°, 30°, 40°, 43°, 47°, 50°, 51°, 57°, 60°, 64°, 71° and 78° with reflections from (001), (011), (012), (003), (110), (111), (103), (201), (004), (202), (023), and (121) planes, respectively. It should be noted that 1-S sample shows a small peak of unreacted Selenium (Se) at 2θ=23°. All the XRD peaks match closely with the standard JCPDS Card No. 089-2939.

For 2-SG sample, $SnSe_2$-rGO, with 0.4% rGO introduced, the XRD pattern can be seen in the Figure 4.1. The third peak from the bottom, marked 2-SG, in blue, shows the XRD patterns of 2-SG. It can be seen that the peaks from 1-S are replicated here with the exception of the peak of unreacted Se, which in this case, does not appear, meaning, no traces of unreacted Se were found. The XRD peaks again show sharp patterns at 2θ angles of 14°, 28°, 30°, 40°, 43°, 47°, 50°, 51°, 57°, 60°, 64°, 71° and 78° with reflections from (001), (100), (011), (012), (003), (110), (111), (103), (201), (004), (202), (023), and (121) planes, respectively. Considering the concentration of rGO is too less in this composite, XRD peak for rGO cannot be seen as XRD requires at least 6% concentration of a constituent, in order to be detected.

For 3-SG, the composite is again $SnSe_2$-rGO but this time, with 5.7% rGO concentration. The peaks in this case again are the same as 2-SG with no traces of unreacted Se. And again, as the concentration of rGO is below 6%, no peak can be seen to identify the presence of rGO in the composite sample 3-SG. The rest of the peaks and the planes are the same as 2-SG.

Finally, when it comes to 4-SG, the $SnSe_2$-rGO composite, this time has an rGO concentration of 11.7% which is sufficiently high. The rest of the peaks match as those of 2-SG and 3-SG, appearing at the same angles and reflections of the same planes. However, in this case, a peak appears at 2θ=26° and has reflection from (002) plane, which shows the presence of rGO in this sample as it has a concentration which is higher than minimum threshold required for XRD i.e. 6%. 4-SG confirms the formation of $SnSe_2$-rGO

composite with no impurities. For 2-SG and 3-SG, the presence of rGO can be confirmed through SEM images in the next section.

4.2 Morphological Analysis (SEM)

The morphological study of the samples was carried out using a Scanning Electron Microscope (SCME, NUST) for all the samples. The SEM images of the samples can be seen in Figure 4.2 in this section.

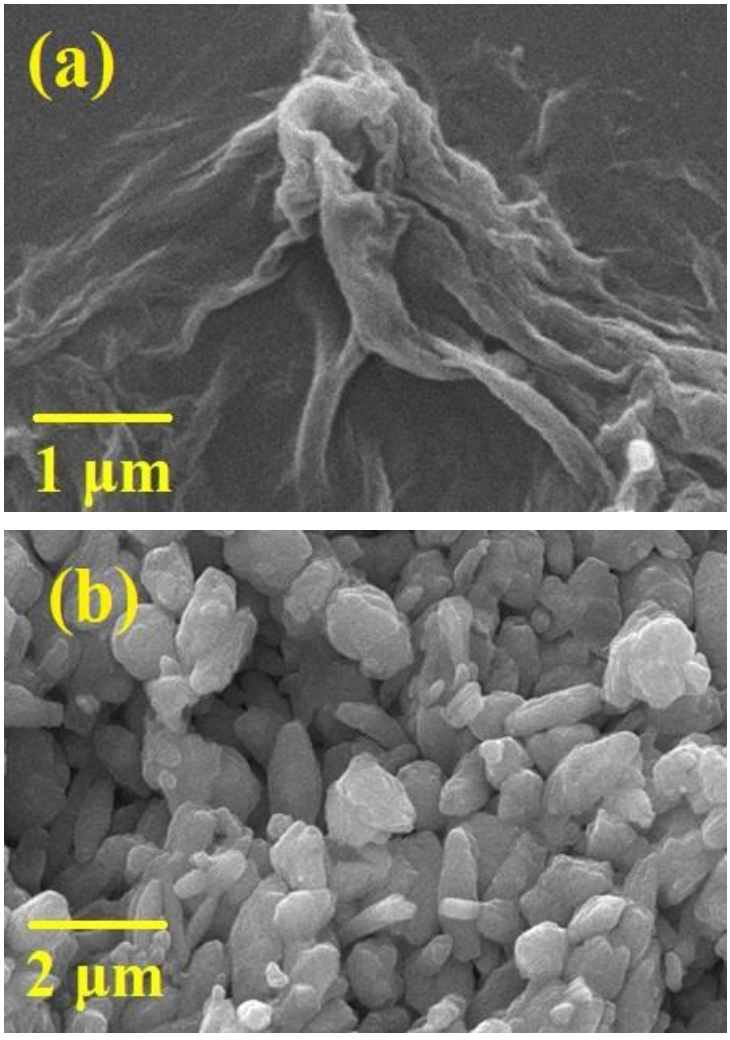

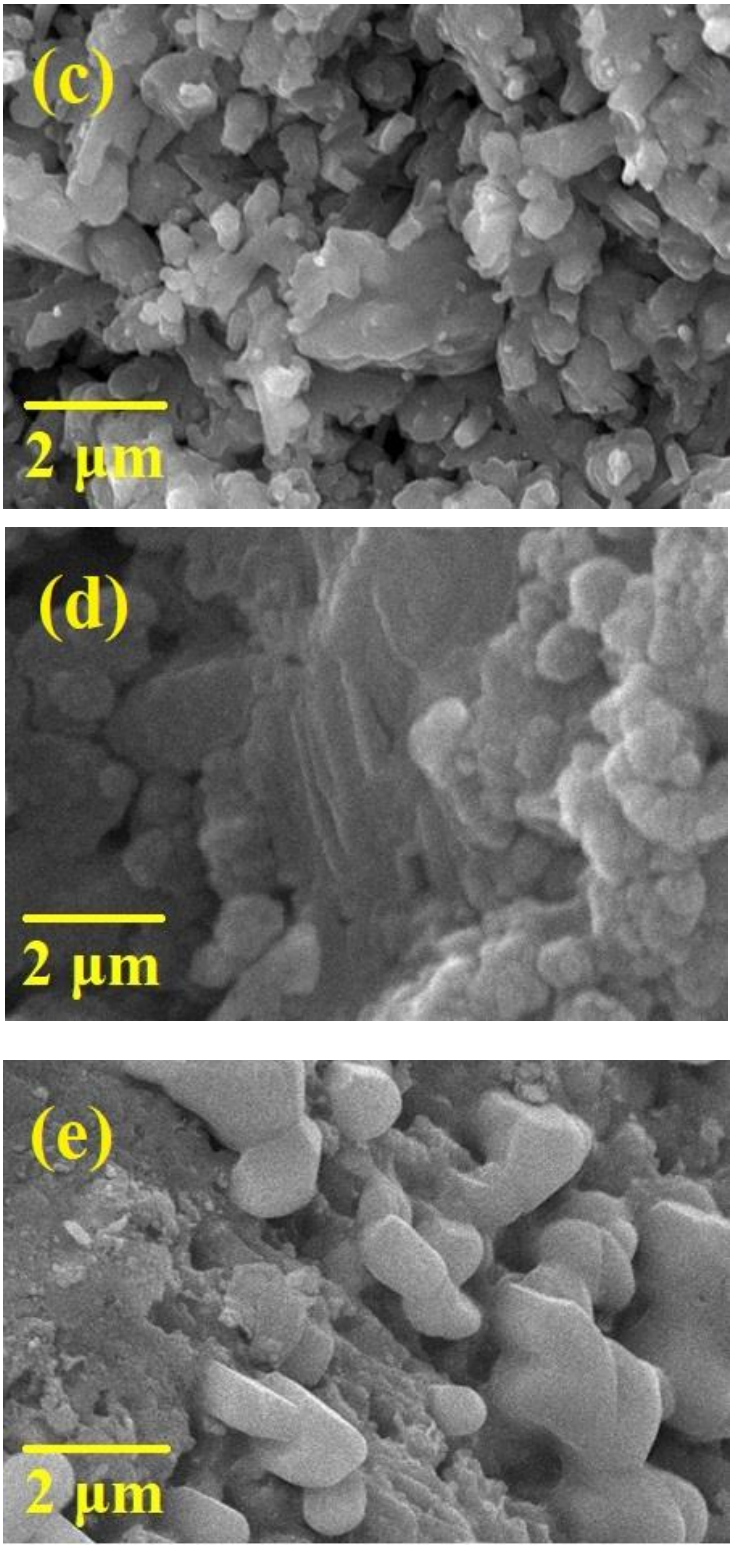

Figure 4.2 SEM Images of the samples **(a)** rGO, **(b)** 1-S, **(c)** 2-SG, **(d)** 3-SG and **(e)** 4-SG

It should be noted that for SEM analysis, the pellet samples were cut in the middle in order to be able to observe the cross-section for analyzing the internal structure of the sample and ensure the observation of the presence of rGO and the composite formation.

As can be seen from Figure 4.2(a), which is the SEM image of GO, it shows a thin membrane or curtain-like structure which is shows a spread structure. This image was taken at the resolution of 1 μm. Figure 4.2(b) shows a SEM image of 1-S or pure $SnSe_2$ at a resolution of 2 μm. The structure, as can be seen from the image, shows rod-like structure with some traces of flower-like structure as well, as if the rods have come together and gotten attached to each other. Figure 4.3 (c) shows the SEM image of 2-SG or $SnSe_2$-rGO (rGO = 0.4%) and it can be seen from the image that there is a presence of rGO in the composite while the $SnSe_2$ rods and particles have grown into the rGO particles, ensuring the formation of $SnSe_2$-rGO composite. In Figure 4.2 (d), we can see that SEM image for 3-SG or $SnSe_2$-rGO (rGO = 5.7%) at a resolution of 2 μm. The image displays that the particle size of rGO is comparatively bigger with more growth of $SnSe_2$ into the rGO particles. The resolution for this image was again 2 μm. Finally, Figure 4.2 (e) shows an image of 4-SG or $SnSe_2$-rGO (rGO = 11.7%) at a resolution of 2 μm. It can be seen that the rod-like particles of $SnSe_2$ have grown into the rGO particles and the composite formation can be seen here more clearly.

4.3 UV-Visible Spectrophotometry

UV-Vis analysis was conducted for 4 samples which were the subject of the research and were designed for studying the thermoelectric properties. The samples used were pure $SnSe_2$ and $SnSe_2$-rGO composites, in the form of 1-S, 2-SG, 3-SG and 4-SG. As can be seen from Figure 4.4, it shows the graph for all 4 samples. According to Figure 4.4, it can be seen that the absorption peak for 1-S lies at a wavelength of 1341 nm. Similarly, it can be seen that the absorption peak for 2-SG lies at 1348 nm which is a bit further than 1-S, portraying a narrower bandgap. As we move to sample 3-SG, the absorption peak lies at the wavelength of 1356 nm. Finally, the absorption peak for 4-SG lies at 1369 nm and is the highest on the wavelength scale.

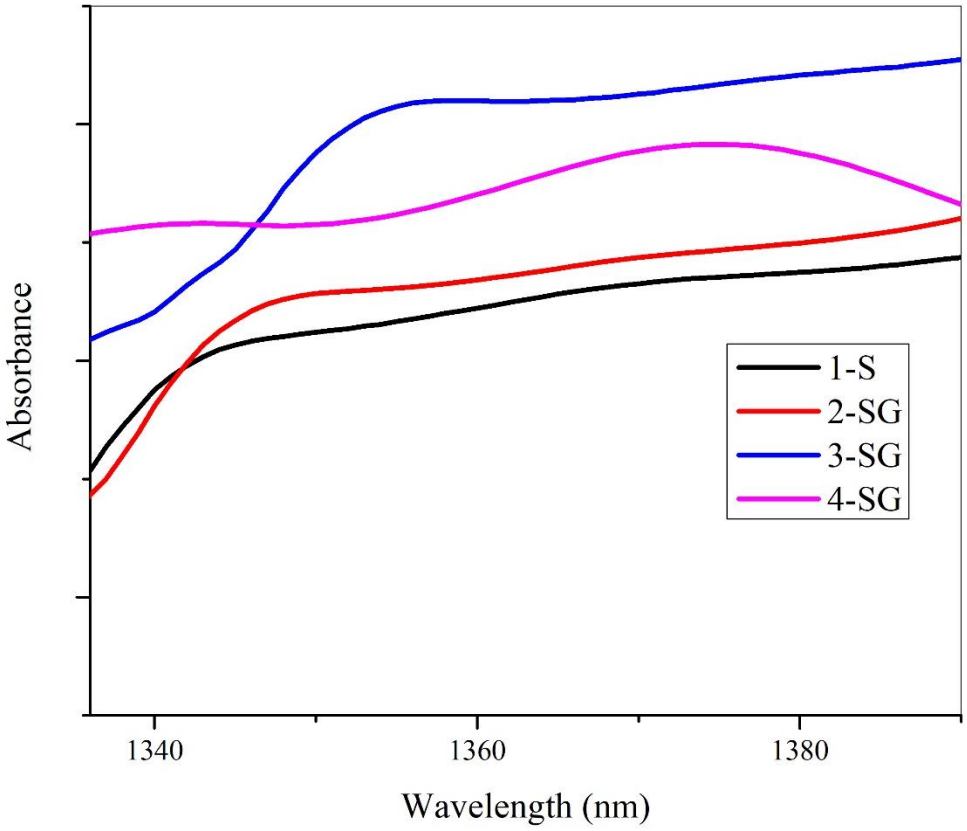

Figure 4.3 UV-Vis Spectra of pellet samples 1-S, 2-SG, 3-SG and 4-SG

4.3.1 Bandgap Analysis

Using the data from the UV-Vis Spectrophotometry, bandgap of the samples was calculated. The bandgap can be calculated by using the absorption and wavelength from the UV-Vis spectra. Wavelength is used to calculate the energy (hv). Absorption can be used to calculate the absorbance coefficient or α. After calculating both these, square root of their product (α x hv) was taken. Finally, a graph was then plotted with $(\alpha.hv)^{1/2}$ on y-axis and hv on x-axis.

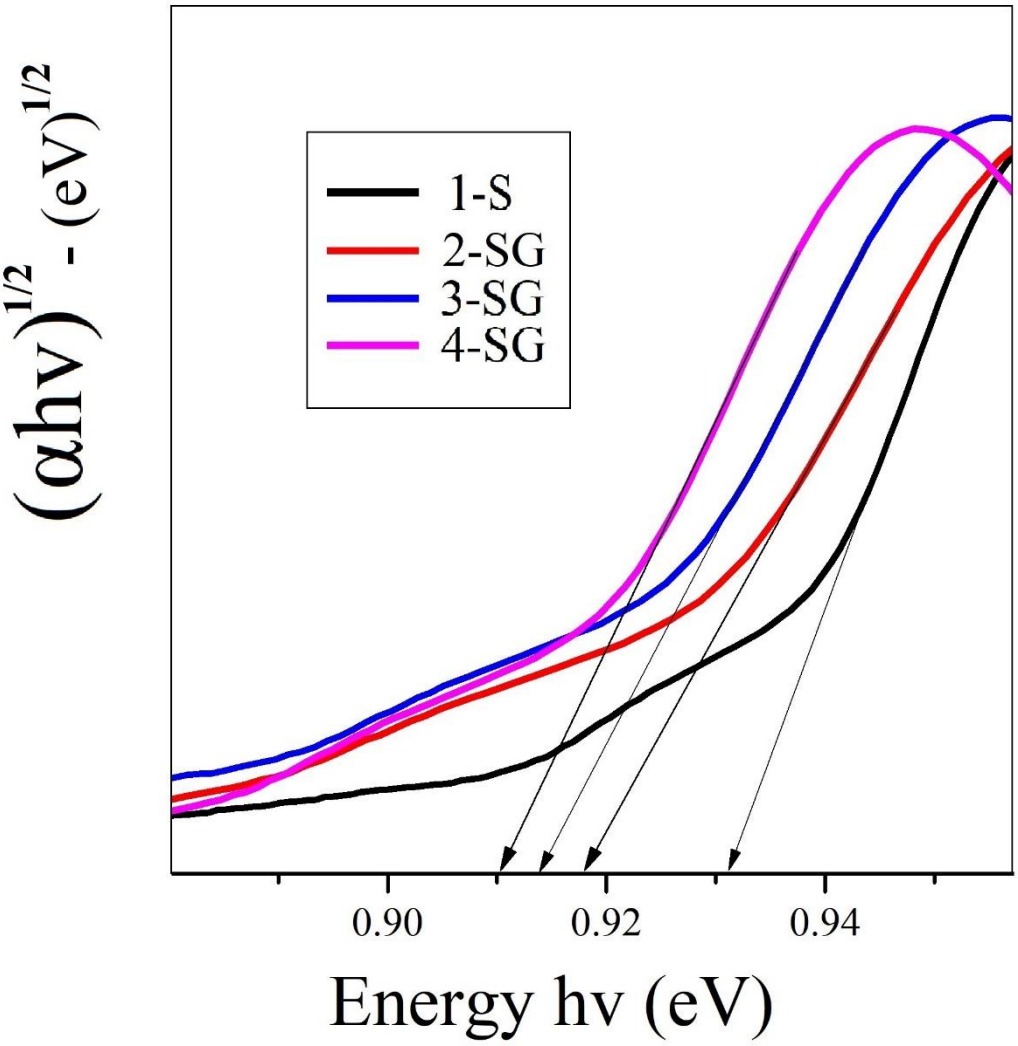

Figure 4.4 Bandgap Analysis of pellet samples 1-S, 2-SG, 3-SG and 4-SG

Figure 4.5 shows a combined image of bandgaps of all 4 samples i.e. 1-S, 2-SG, 3-SG and 4-SG. It can be seen from the figure that 1-S, which is pure $SnSe_2$, has a bandgap of 0.931eV. As we go to 2-SG, where 0.4% rGO is added to $SnSe_2$, the bandgap shows a considerable improvement and gets narrower, reaching a value of 0.918eV. When we come to 3-SG, the concentration of rGO in $SnSe_2$ is even higher, at 5.7% but the impact on bandgap is not so drastic in comparison as it comes down to 0.914eV which is a minor improvement. Finally, when we calculate the bandgap for 4-SG, where rGO is 11.7%, the

improvement again is not so noteworthy and it brings the bandgap down to 0.91eV, which again, is not a notable improvement when compared to improvement shown in 2-SG.

From this analysis, it can be asserted that the increasing concentration of rGO in $SnSe_2$ had an effect on the bandgap and it helped in narrowing it down. However, when we analyze in detail, we can see that the as the concentration of rGO is increased, the trend of improvement in bandgap starts to scale down. As can be seen, in 2-SG, 0.4% rGO improved the bandgap from 0.931eV to 0.918eV which is a drastic change but as we move on to 3-SG and 4-SG, although the concentration of rGO is improved by big multiples in comparison to 2-SG, the improvement in bandgap is not proportional to that. This gives us information that at one point, the addition of rGO will no longer help improve the bandgap of $SnSe_2$ and may start having adverse impact on the properties.

4.4 Hall Effect Measurement

Hall measurement of the samples 1-S, 2-SG, 3-SG and 4-SG was taken at room temperature i.e. 300K. The results of the measurement can be seen in Table 4.1.

It has been reported by Pham et. al. that a maximum value of carrier concentration achieved was 2.26 $x10^{18}$ cm^{-3} at 300K [93]. This resulted in a lower electrical conductivity. As a result of the addition of graphene, the maximum value for carrier concentration achieved at room temperature (300K) was 2.94 $x10^{18}$ cm^{-3} which is a considerable improvement.

Table 4.1 Hall Carrier Concentration and Mobility of the pellet samples 1-S, 2-SG, 3-Sg and 4-SG, at room temperature i.e. 300K

Sample #	**Temperature (K)**	**Carrier Concentration n (cm^{-3})**	**Carrier Mobility ($cm^2.v^{-1}.s^{-1}$)**
1-S	300	2.1 $x10^{18}$	31.6
2-SG	300	2.5 $x10^{18}$	30.71
3-SG	300	2.73 $x10^{18}$	30.05
4-SG	300	2.94 $x10^{18}$	29.41

It can be seen from the table that with increasing concentration of rGO in $SnSe_2$, the Hall carrier concentration keeps on increasing while the hall mobility decreases as a result of that. It can be further noticed that the effect of the increasing concentration of rGO on the improvement in carrier concentration, displays a downwards trend. The measurement asserts that the increasing concentration of rGO will have a negligible or no effect at one point in time and might even affect the properties in a negative way.

4.5 Thermoelectric Properties

The thermoelectric properties were measured for all 4 samples to see the improvement after introduction of graphene in $SnSe_2$. Pham et. al. performed a study in 2020, which has been used as a reference in this research to analyze our results against. Electrical conductivity, Seebeck, Thermal conductivity and ZT were obtained as a result of the analysis. These properties are discussed below.

4.5.1 Electrical Conductivity

Pham et. al. reported a maximum value of 750 S/m along the c-axis for $SnSe_2$ single crystal, in its pure form [93]. As a result of this lower thermal conductivity, ZT of $SnSe_2$ was compromised. It can be seen here that the addition of graphene enhanced the electrical conductivity by a very considerable margin as it reached a maximum value of 2479 S/m for 4-SG, which is the desired outcome.

The effect of rGO on electrical conductivity of $SnSe_2$ is very noticeable as can be seen in Figure 4.6. It can be seen that for 4-SG, the electrical conductivity is the highest at room temperature, coming in at 2479 S/m. and reaches a minimum value of 1188 S/m with increasing temperature. For 3-SG, the maximum value recorded was 1705 S/m at room temperature while the minimum was at 1061 S/m, at 750K. 2-SG, having the minimum rGO concentration of 0.4%, displayed a maximum value 1204 S/m at 300K and kept on decreasing, reaching 740 S/m at 750K. When it comes to pure $SnSe_2$, 1-S, the maximum value recorded was at 300K of 465 S/m and at 750K, it went down to 385 S/m.

The above data provides us with information about the behavior of $SnSe_2$ as the concentration of rGO increases and also tells us about the effect of temperature on electrical conductivity of all the samples. The overall trend when it comes to temperature increase, is downward as the electrical conductivity for all 4 samples keeps on decreasing with increasing temperature. However, it's effect on pure $SnSe_2$ is minimum compared to other 3 samples with rGO involved.

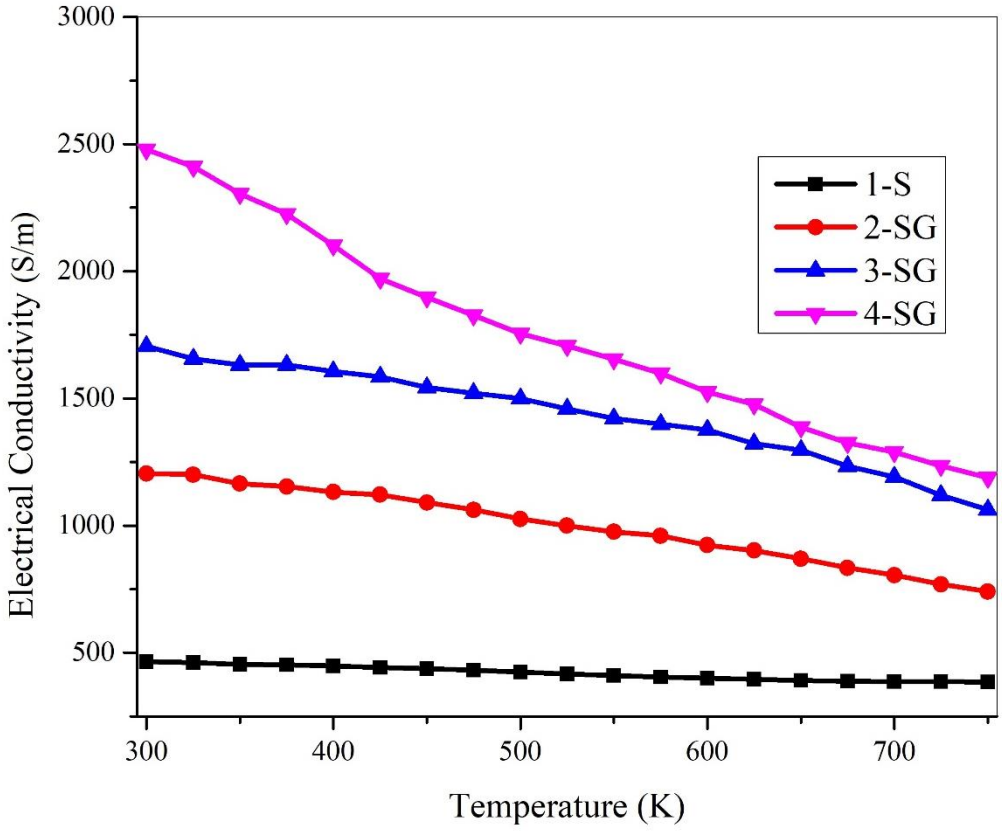

Figure 4.5 Effect of rGO and increasing Temperature on electrical conductivity of $SnSe_2$

It can be further noted that the addition of graphene brings a drastic change in electrical conductivity. We can see from the figure that the introduction of 0.4% rGO had a major effect on the electrical conductivity of $SnSe_2$, however, when the concentration of rGO was increased, this effect kept on reducing in magnitude. This gives us an idea that higher

concentrations of graphene will have a negligible effect on the electrical conductivity of $SnSe_2$ and can affect the properties as well.

4.5.2 Seebeck Coefficient

Seebeck coefficient has an inverse relationship with electrical conductivity and as a result, with increasing electrical conductivity, Seebeck reduces. This is because Seebeck is inversely related to charge carrier concentration while it is directly related to carrier mobility, hence, it has an inverse relationship with electrical conductivity as well. Figure 4.7 depicts the same as can be seen. The trend in this case is reversed as it can be seen that with increasing temperature, the Seebeck coefficient keeps on increasing but with increasing concentration of rGO, the Seebeck reduces. At the same time, 1-S shows a decline in Seebeck after 675K as after this point, the sample displays a thermally activated transport behavior.

Pham et. al. reported the same trend in their research stating that till 500K, the sample displays a metallic transport behavior and as a result of that, it shows an increase in the Seebeck value as we move along the x-axis. Once we reach 500K, the transport behavior becomes thermally activated which causes a fall in the Seebeck [93]. The maximum value reported by Pham et. al. is -350 μV/K (n-type) [93].

Addition of rGO increases the conduction and metallic behavior limit and that's why, the same trend is not seen in the rest of the samples. The addition of rGO in smaller concentration has a major effect but this time, in a negative way and as the concentration of rGO is increased in 3-SG and 4-SG, the impact is not so drastic. The drop in Seebeck is due to increasing carrier concentration as it affects the carrier mobility and that in turn impacts the Seebeck overall. The increasing trend in regards to the temperature is for the same reason, as higher temperatures provide energy to the charges and as a result, the mobility somehow improves.

It should be noted that the negative sign in Figure 4.7 depicts that the analysis was conducted for n-type semiconductors. The maximum value of Seebeck coefficient is achieved by 1-S, of -420 μV/K at a temperature of 675K while the minimum value at

highest temperature is that of 4-SG which was recorded at -239 μV/K. Although the drop in Seebeck value does affect the overall ZT, this drop is not as effective compared to the increased in electrical conductivity and as a result, the overall power factor is enhanced with the introduction of rGO.

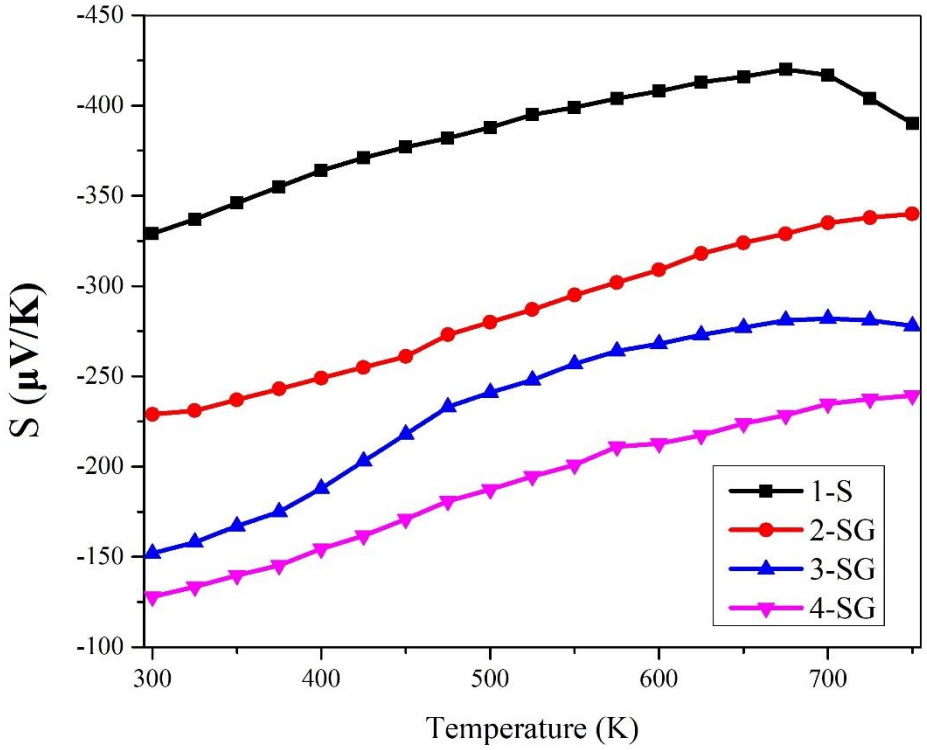

Figure 4.6 Effect of rGO and increasing Temperature on Seebeck coefficient of $SnSe_2$

4.5.3 Thermal Conductivity

The behavior of thermal conductivity is illustrated in Figure 4.8 which shows a decreasing trend with increasing temperature.

Being in the denominator, the lower the value of thermal conductivity, the better it is for overall ZT. Although the increasing concentration of rGO increases the thermal conductivity of $SnSe_2$, it can still be seen that 2-SG and 3-SG reach lower values than pure $SnSe_2$ at temperatures beyond 700K.

Thermal conductivity for pure $SnSe_2$ has been reported by Pham et. al. and according to that research, along c-axis, the thermal conductivity stood at 1 W/m.K as its maximum value [93]. In our research, the thermal conductivity of $SnSe_2$ stood at 1.05 W/m.K and it kept on increasing with the addition of rGO reaching a maximum value of 1.63 W/m.K.

It should be noted that the overall increase in thermal conductivity of the samples is lower in comparison to the increase caused by introduction of rGO in electrical conductivity. This is due to phonon scattering, as was explained in Chapter 2. Total thermal conductivity is the sum of lattice thermal conductivity and electronic thermal conductivity. The introduction of graphene causes phonon scattering and as a result, the lattice thermal conductivity of $SnSe_2$ decreases which in turn controls the total thermal conductivity, making this introduction favorable for the desired purpose of research.

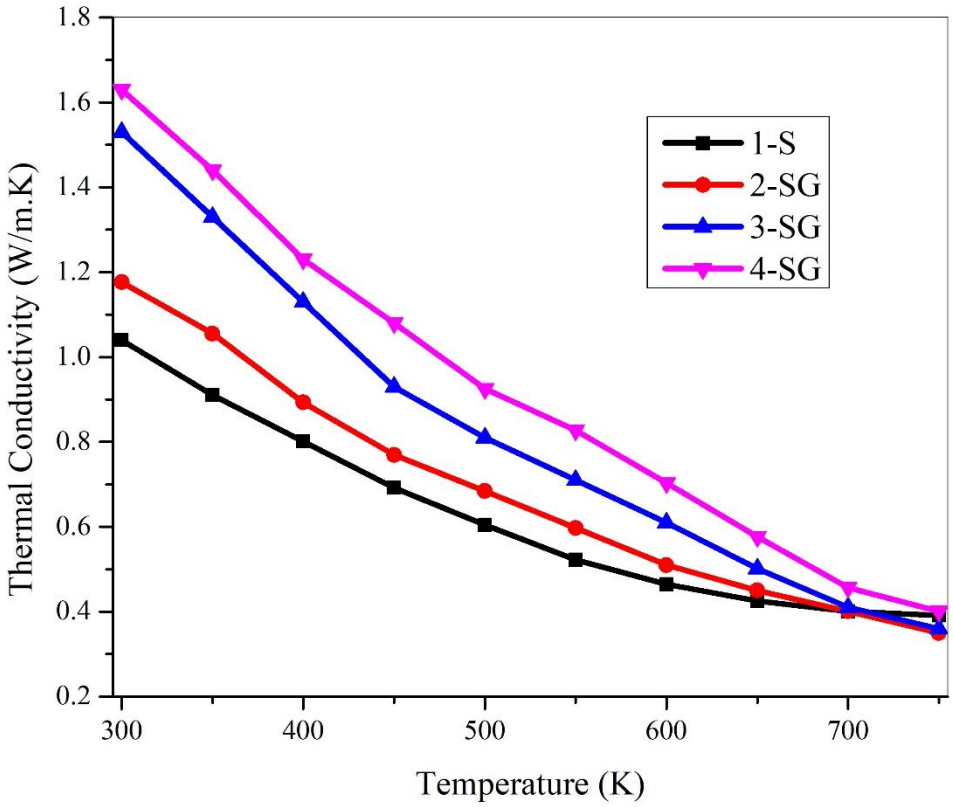

Figure 4.7 Effect of rGO and increasing Temperature on thermal conductivity of $SnSe_2$

4.5.4 Figure of Merit (ZT)

Finally, coming to the ZT or the overall efficiency of the designed samples, we can see the trend and the overall behavior of ZT with increasing temperature and increasing concentration of rGO in Figure 4.9.

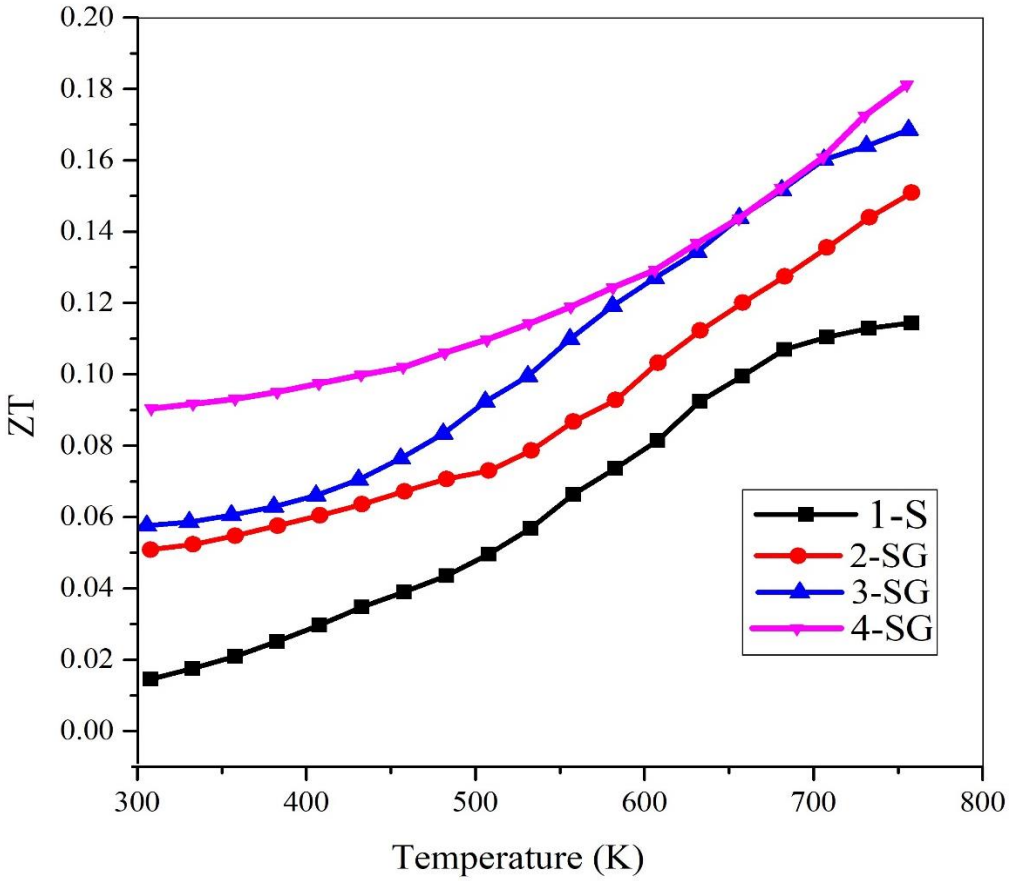

Figure 4.8 Effect of rGO and increasing Temperature on the ZT of $SnSe_2$

A ZT value of 0.15 has been achieved for pure $SnSe_2$ according to a research carried out by Pham et. al [93]. This shows that $SnSe_2$ is a promising contender among TE materials and its TE properties can be enhanced through various methods. As discussed in this thesis, rGO was used as one method to enhance its TE properties by making a composite. The results achieved were promising and showed a significant improvement, reaching a maximum ZT value of 0.18.

The overall trend with respect to temperature portrays that with increasing temperature, ZT of the sample keeps on increasing but the slope of the curve decreases when the temperature reaches 750K, showing that further increase in temperature will have a minor effect on the ZT and might even cause the ZT value to drop. At the same time, it can also be seen that the increasing concentration of rGO enhances the overall ZT which means that introduction of rGO had a positive impact on the TE properties of $SnSe_2$.

It can be seen from the figure below, that the maximum ZT value achieved for pure $SnSe_2$ is 0.11 at 750K. For 2-SG, the maximum value achieved is 0.15 which is considerably higher than that of pure $SnSe_2$. For 3-SG, the maximum ZT achieved is 0.17 while the same for 4-SG is 0.18. It can be observed that the overall enhancement is impressive and hence, can be deduced that the addition of rGO has a positive impact on the TE properties of $SnSe_2$. However, at the same time, another important thing to note is that the increasing concentration of rGO does not reflect the same increase in the ZT value but rather, the increase is minor compared to the increase shown by 2-SG at rGO = 0.4%, which is 0.04. The change in ZT of 2-SG and 3-SG is 0.02 while that between 3-SG and 4-SG is only 0.01. It can be further noticed that in 4-SG, the curve shows a different behavior and has a slower increase in ZT compared to the other 3 samples. This gives us an idea that the increasing concentration of rGO has a declining impact on the overall ZT properties of $SnSe_2$.

CHAPTER 5 CONCLUSION

Considering the cost-effectiveness and environmental friendliness of $SnSe_2$, this compound was chosen for the research. And after material selection, we were able to synthesize $SnSe_2$ and $SnSe_2$-rGO in a cost-effective way. After the synthesis, the material was then characterized, morphological studies were carried out and the TE properties of the sample were studied. The results thereby have shown that the maximum ZT value achieved, stood at 0.18 which is an improvement from the ZT value of 0.11 that is possessed by pure $SnSe_2$. It was also observed that addition of rGO enhanced the electrical conductivity in an impressive way. However, it should be noted that the increasing concentration of rGO, even though had a positive impact, still, as the concentration was increased stepwise, the impact on TE properties was not proportional to the increase in concentration. The results obtained through this research show that the ZT of $SnSe_2$ can be improved by introduction of rGO and it can be used in the future for TE applications, with other enhancements.

REFERENCES

[1] Finn, B. S. (1967). Thomson's dilemma. *Physics Today*, *20*(9), 54. doi:https://doi.org/10.1063/1.3034483

[2] Minnich, A. J., Dresselhaus, M. S., Ren, Z. F., & Chen, G. (2009). Bulk nanostructured thermoelectric materials: Current research and future prospects. *Energy & Environmental Science*, *2*(5), 466. doi:10.1039/b822664b

[3] Disalvo, F. J. (1999). Thermoelectric Cooling and Power Generation. *Science*, *285*(5428), 703-706. doi:10.1126/science.285.5428.703

[4] Mahan, G. D. (2016). Introduction to thermoelectrics. *APL Materials*, *4*(10), 104806. doi:10.1063/1.4954055

[5] Rowe, D. (2005). General Principles and Basic Considerations. *Thermoelectrics Handbook*. doi:10.1201/9781420038903.sec1

[6] Ding, G., Gao, G., & Yao, K. (2015). High-efficient thermoelectric materials: The case of orthorhombic IV-VI compounds. *Scientific Reports*, *5*(1). doi:10.1038/srep09567

[7] Bell, L. E. (2008). Cooling, Heating, Generating Power, and Recovering Waste Heat with Thermoelectric Systems. *Science*, *321*(5895), 1457-1461. doi:10.1126/science.1158899

[8] British Petrolume, BP Statistical Review of World Energy June 2012 (bp.com/statisticalreview) (2012), pp. 1–48

[9] Q. H. Escobedo, F. M. Agugliaro, J. A. G. Parra, and A. Z. Sierra, Renew. Sustain. Energy Rev. 15, 721 (2011)

[10] Alam, H., & Ramakrishna, S. (2013). A review on the enhancement of figure of merit from bulk to nano-thermoelectric materials. *Nano Energy*, *2*(2), 190-212. doi:10.1016/j.nanoen.2012.10.005

[11] Zhao, D., & Tan, G. (2014). A review of thermoelectric cooling: Materials, modeling and applications. *Applied Thermal Engineering*, *66*(1-2), 15-24. doi:10.1016/j.applthermaleng.2014.01.074

[12] Martín-González, M., Caballero-Calero, O., & Díaz-Chao, P. (2013). Nanoengineering thermoelectrics for 21st century: Energy harvesting and other trends in the field. *Renewable and Sustainable Energy Reviews*, *24*, 288-305. doi:10.1016/j.rser.2013.03.008

[13] Shakouri, A. (2011). Recent Developments in Semiconductor Thermoelectric Physics and Materials. *Annual Review of Materials Research, 41*(1), 399-431. doi:10.1146/annurev-matsci-062910-100445

[14] Snyder, G. J., & Toberer, E. S. (2008). Complex thermoelectric materials. *Nature Materials, 7*(2), 105-114. doi:10.1038/nmat2090

[15] Yadav, G. G., Zhang, G., Qiu, B., Susoreny, J. A., Ruan, X., & Wu, Y. (2011). Self-templated synthesis and thermal conductivity investigation for ultrathin perovskite oxide nanowires. *Nanoscale, 3*(10), 4078. doi:10.1039/c1nr10624d

[16] Protsak, I. S., Champet, S., Chiang, C., Zhou, W., Popuri, S. R., Bos, J. G., . . . Gregory, D. H. (2019). Toward New Thermoelectrics: Tin Selenide/Modified Graphene Oxide Nanocomposites. *ACS Omega, 4*(3), 6010-6019. doi:10.1021/acsomega.8b03146

[17] Simons, R., & Chu, R. (n.d.). Application of thermoelectric cooling to electronic equipment: A review and analysis. *Sixteenth Annual IEEE Semiconductor Thermal Measurement and Management Symposium (Cat. No.00CH37068)*. doi:10.1109/stherm.2000.837055

[18] Nolas, G. S., Sharp, J., & Goldsmid, H. J. (2001). Thermoelectrics. *Springer Series in MATERIALS SCIENCE*. doi:10.1007/978-3-662-04569-5

[19] Nolas, G. S., Poon, J., & Kanatzidis, M. (2006). Recent Developments in Bulk Thermoelectric Materials. *MRS Bulletin, 31*(3), 199-205. doi:10.1557/mrs2006.45

[20] Elsheikh, M. H., Shnawah, D. A., Sabri, M. F., Said, S. B., Hassan, M. H., Bashir, M. B., & Mohamad, M. (2014). A review on thermoelectric renewable energy: Principle parameters that affect their performance. *Renewable and Sustainable Energy Reviews, 30*, 337-355. doi:10.1016/j.rser.2013.10.027

[21] Riffat, S., & Ma, X. (2003). Thermoelectrics: A review of present and potential applications. *Applied Thermal Engineering, 23*(8), 913-935. doi:10.1016/s1359-4311(03)00012-7

[22] Kishi, M., Nemoto, H., Hamao, T., Yamamoto, M., Sudou, S., Mandai, M., & Yamamoto, S. (n.d.). Micro thermoelectric modules and their application to wristwatches as an energy source. *Eighteenth International Conference on Thermoelectrics. Proceedings, ICT99 (Cat. No.99TH8407)*. doi:10.1109/ict.1999.843389

[23] Snyder, G. J. (2008). Small Thermoelectric Generators. *The Electrochemical Society Interface, 17*(3), 54-56. doi:10.1149/2.f06083if

[24] Tritt, T. M. (2012). ChemInform Abstract: Thermoelectric Phenomena, Materials, and Applications. *ChemInform, 43*(10). doi:10.1002/chin.201210227

[25] Bell, L. E. (2008). Cooling, Heating, Generating Power, and Recovering Waste Heat with Thermoelectric Systems. *Science, 321*(5895), 1457-1461. doi:10.1126/science.1158899

[26] Shi, X., Yang, J., Salvador, J. R., Chi, M., Cho, J. Y., Wang, H., . . . Chen, L. (2012). Multiple-Filled Skutterudites: High Thermoelectric Figure of Merit through Separately Optimizing Electrical and Thermal Transports. *Journal of the American Chemical Society*, *134*(5), 2842-2842. doi:10.1021/ja211185w

[27] Li, J., Liu, W., Zhao, L., & Zhou, M. (2010). High-performance nanostructured thermoelectric materials. *NPG Asia Materials, 2*(4), 152-158. doi:10.1038/asiamat.2010.138

[28] Zhao, D., & Tan, G. (2014). A review of thermoelectric cooling: Materials, modeling and applications. *Applied Thermal Engineering, 66*(1-2), 15-24. doi:10.1016/j.applthermaleng.2014.01.074

[29] Alsalama, M., Hamoudi, H., & Youssef, K. M. (2021). The effect of graphene structural integrity on the power factor of tin selenide nanocomposite. *Journal of Alloys and Compounds, 872*, 159584. doi:10.1016/j.jallcom.2021.159584

[30] Qiu, Y., Xi, L., Shi, X., Qiu, P., Zhang, W., Chen, L., . . . Snyder, G. J. (2013). Charge-Compensated Compound Defects in Ga-containing Thermoelectric Skutterudites. *Advanced Functional Materials, 23*(25), 3194-3203. doi:10.1002/adfm.201202571

[31] Bai, S., Pei, Y., Chen, L., Zhang, W., Zhao, X., & Yang, J. (2009). Enhanced thermoelectric performance of dual-element-filled skutterudites BaxCeyCo4Sb12. *Acta Materialia, 57*(11), 3135-3139. doi:10.1016/j.actamat.2009.03.018

[32] Toberer, E. S., May, A. F., Scanlon, C. J., & Snyder, G. J. (2009). Thermoelectric properties of p-type LiZnSb: Assessment of ab initio calculations. *Journal of Applied Physics, 105*(6), 063701. doi:10.1063/1.3091267

[33] Fu, C., Zhu, T., Pei, Y., Xie, H., Wang, H., Snyder, G. J., . . . Zhao, X. (2014). High Band Degeneracy Contributes to High Thermoelectric Performance in p-Type Half-Heusler Compounds. *Advanced Energy Materials, 4*(18), 1400600. doi:10.1002/aenm.201400600

[34] Horák, J., Stary, Z., Lošťák, P., & Pancíř, J. (1990). Anti-site defects in n-Bi2Se3 crystals. *Journal of Physics and Chemistry of Solids, 51*(12), 1353-1360. doi:10.1016/0022-3697(90)90017-a

[35] Starý, Z., Horák, J., Stordeur, M., & Stölzer, M. (1988). Antisite defects in Sb2−xBixTe3 mixed crystals. *Journal of Physics and Chemistry of Solids, 49*(1), 29-34. doi:10.1016/0022-3697(88)90130-8

[36] Kumar, G. S., Prasad, G., & Pohl, R. O. (1993). Experimental determinations of the Lorenz number. *Journal of Materials Science, 28*(16), 4261-4272. doi:10.1007/bf01154931

[37] Kim, H., Gibbs, Z. M., Tang, Y., Wang, H., & Snyder, G. J. (2015). Characterization of Lorenz number with Seebeck coefficient measurement. *APL Materials, 3*(4), 041506. doi:10.1063/1.4908244

[38] Shakouri, A. (2011). Recent Developments in Semiconductor Thermoelectric Physics and Materials. *Annual Review of Materials Research, 41*(1), 399-431. doi:10.1146/annurev-matsci-062910-100445

[39] Toberer, E. S., May, A. F., & Snyder, G. J. (2009). Zintl Chemistry for Designing High Efficiency Thermoelectric Materials. *Chemistry of Materials, 22*(3), 624-634. doi:10.1021/cm901956r

[40] Zhu, T., Liu, Y., Fu, C., Heremans, J. P., Snyder, J. G., & Zhao, X. (2017). Compromise and Synergy in High-Efficiency Thermoelectric Materials. *Advanced Materials, 29*(30). doi:10.1002/adma.201702816

[41] Zhao, L., Dravid, V. P., & Kanatzidis, M. G. (2014). The panoscopic approach to high performance thermoelectrics. *Energy Environ. Sci., 7*(1), 251-268. doi:10.1039/c3ee43099e

[42] Zhang, Q., Liao, B., Lan, Y., Lukas, K., Liu, W., Esfarjani, K., . . . Ren, Z. (2013). High thermoelectric performance by resonant dopant indium in nanostructured SnTe. *Proceedings of the National Academy of Sciences, 110*(33), 13261-13266. doi:10.1073/pnas.1305735110

[43] Nethravathi, C., Rajamathi, C. R., Rajamathi, M., Maki, R., Mori, T., Golberg, D., & Bando, Y. (2014). Synthesis and thermoelectric behaviour of copper telluride nanosheets. *J. Mater. Chem. A, 2*(4), 985-990. doi:10.1039/c3ta12877f

[44] Callaway, J. (1959). Model for Lattice Thermal Conductivity at Low Temperatures. *Physical Review, 113*(4), 1046-1051. doi:10.1103/physrev.113.1046

[45] Callaway, J., & Baeyer, H. C. (1960). Effect of Point Imperfections on Lattice Thermal Conductivity. *Physical Review, 120*(4), 1149-1154. doi:10.1103/physrev.120.1149

[46] Abeles, B. (1963). Lattice Thermal Conductivity of Disordered Semiconductor Alloys at High Temperatures. *Physical Review, 131*(5), 1906-1911. doi:10.1103/physrev.131.1906

[47] Qiu, P., Shi, X., & Chen, L. (2016). Cu-based thermoelectric materials. *Energy Storage Materials, 3*, 85-97. doi:10.1016/j.ensm.2016.01.009

[48] He, J., & Tritt, T. M. (2017). Advances in thermoelectric materials research: Looking back and moving forward. *Science, 357*(6358). doi:10.1126/science.aak9997

[49] Sales, B. C., Mandrus, D., & Williams, R. K. (1996). Filled Skutterudite Antimonides: A New Class of Thermoelectric Materials. *Science, 272*(5266), 1325-1328. doi:10.1126/science.272.5266.1325

[50] Ohta, H. (2007). Thermoelectrics based on strontium titanate. *Materials Today, 10*(10), 44-49. doi:10.1016/s1369-7021(07)70244-4

[51] Zhang, L. (2018). Investigation of Tin Chalcogenides Thermoelectric Materials for Energy Conversion, Doctor Philosophy thesis, Institute for Superconducting and Electronic Materials (ISEM), University of Wollongong.

[52] Hu, L., Wu, H., Zhu, T., Fu, C., He, J., Ying, P., & Zhao, X. (2015). Tuning Multiscale Microstructures to Enhance Thermoelectric Performance of n-Type Bismuth-Telluride-Based Solid Solutions. *Advanced Energy Materials, 5*(17), 1500411. doi:10.1002/aenm.201500411

[53] Yan, X., Poudel, B., Ma, Y., Liu, W. S., Joshi, G., Wang, H., . . . Ren, Z. F. (2010). Experimental Studies on Anisotropic Thermoelectric Properties and Structures of n-Type Bi2Te2.7Se0.3. *Nano Letters, 10*(9), 3373-3378. doi:10.1021/nl101156v

[54] Chung, D., Hogan, T., Brazis, P., Rocci-Lane, M., Kannewurf, C., Bastea, M., . . . Kanatzidis, M. G. (2010). ChemInform Abstract: CsBi4Te6: A High-Performance Thermoelectric Material for Low-Temperature Applications. *ChemInform, 31*(22). doi:10.1002/chin.200022003

[55] Chung, D., Hogan, T. P., Rocci-Lane, M., Brazis, P., Ireland, J. R., Kannewurf, C. R., . . . Kanatzidis, M. G. (2004). A New Thermoelectric Material: CsBi4Te6. *ChemInform, 35*(33). doi:10.1002/chin.200433018

[56] Pulikkotil, J. J., Singh, D. J., Auluck, S., Saravanan, M., Misra, D. K., Dhar, A., & Budhani, R. C. (2012). Doping and temperature dependence of thermoelectric properties in Mg2(Si,Sn). *Physical Review B, 86*(15). doi:10.1103/physrevb.86.155204

[57] Zhao, L., Tan, G., Hao, S., He, J., Pei, Y., Chi, H., . . . Kanatzidis, M. G. (2015). Ultrahigh power factor and thermoelectric performance in hole-doped single-crystal SnSe. *Science, 351*(6269), 141-144. doi:10.1126/science.aad3749

[58] Zhao, L., Chang, C., Tan, G., & Kanatzidis, M. G. (2016). SnSe: A remarkable new thermoelectric material. *Energy & Environmental Science, 9*(10), 3044-3060. doi:10.1039/c6ee01755j

[59] Li, J., Sui, J., Pei, Y., Barreteau, C., Berardan, D., Dragoe, N., . . . Zhao, L. (2012). A high thermoelectric figure of merit ZT > 1 in Ba heavily doped BiCuSeO oxyselenides. *Energy & Environmental Science, 5*(9), 8543. doi:10.1039/c2ee22622g

[60] Sui, J., Li, J., He, J., Pei, Y., Berardan, D., Wu, H., . . . Zhao, L. (2013). Texturation boosts the thermoelectric performance of BiCuSeO oxyselenides. *Energy & Environmental Science, 6*(10), 2916. doi:10.1039/c3ee41859f

[61] Pei, Y., Wu, H., Wu, D., Zheng, F., & He, J. (2014). High Thermoelectric Performance Realized in a BiCuSeO System by Improving Carrier Mobility through 3D Modulation Doping. *Journal of the American Chemical Society, 136*(39), 13902-13908. doi:10.1021/ja507945h

[62] Kraemer, D., Sui, J., Mcenaney, K., Zhao, H., Jie, Q., Ren, Z. F., & Chen, G. (2015). High thermoelectric conversion efficiency of MgAgSb-based material with hot-pressed contacts. *Energy & Environmental Science, 8*(4), 1299-1308. doi:10.1039/c4ee02813a

[63] Shi, X., Yang, J., Salvador, J. R., Chi, M., Cho, J. Y., Wang, H., . . . Chen, L. (2011). Multiple-Filled Skutterudites: High Thermoelectric Figure of Merit through Separately Optimizing Electrical and Thermal Transports. *Journal of the American Chemical Society, 133*(20), 7837-7846. doi:10.1021/ja111199y

[64] Yang, J., Xi, L., Zhang, W., Chen, L. D., & Yang, J. (2009). Electrical Transport Properties of Filled CoSb3 Skutterudites: A Theoretical Study. *Journal of Electronic Materials, 38*(7), 1397-1401. doi:10.1007/s11664-009-0703-9

[65] Nunna, R., Qiu, P., Yin, M., Chen, H., Hanus, R., Song, Q., . . . Chen, L. (2017). Ultrahigh thermoelectric performance in Cu2Se-based hybrid materials with highly dispersed molecular CNTs. *Energy & Environmental Science, 10*(9), 1928-1935. doi:10.1039/c7ee01737e

[66] Fu, C., Bai, S., Liu, Y., Tang, Y., Chen, L., Zhao, X., & Zhu, T. (2015). Realizing high figure of merit in heavy-band p-type half-Heusler thermoelectric materials. *Nature Communications, 6*(1). doi:10.1038/ncomms9144

[67] Fu, C., Zhu, T., Liu, Y., Xie, H., & Zhao, X. (2015). Band engineering of high-performance p-type FeNbSb based half-Heusler thermoelectric materials for figure of merit zT > 1. *Energy & Environmental Science, 8*(1), 216-220. doi:10.1039/c4ee03042g

[68] Tian, Y., Sakr, M. R., Kinder, J. M., Liang, D., Macdonald, M. J., Qiu, R. L., . . . Gao, X. P. (2012). One-Dimensional Quantum Confinement Effect Modulated Thermoelectric Properties in InAs Nanowires. *Nano Letters*, *12*(12), 6492-6497. doi:10.1021/nl304194c

[69] Bletskan, D. (2016). Electronic structure of 2H-SnSe2: Ab initio modeling and comparison with experiment. *Semiconductor Physics Quantum Electronics and Optoelectronics, 19*(1), 98-108. doi:10.15407/spqeo19.01.098

[70] D.I. Bletskan. (2004). Crystalline and Glassy Chalcogenides of Si, Ge, Sn and Alloys on their Base. *Zakarpattia*, Uzhhorod.

[71] Pałosz, B., Gierlotka, S., & Lévy, F. (1985). Polytypism of SnSe2 crystals grown by chemical transport: Structures of six large-period polytypes of SnSe2. *Acta Crystallographica Section C Crystal Structure Communications, 41*(10), 1404-1406. doi:10.1107/s0108270185007958

[72] Pałosz, B., & Salje, E. (1989). Lattice parameters and spontaneous strain in AX 2 polytypes: CdI2, PbI2 SnS2 and SnSe2. *Journal of Applied Crystallography, 22*(6), 622-623. doi:10.1107/s0021889889006916

[73] Au-Yang, M. Y., & Cohen, M. L. (1969). Electronic Structure and Optical Properties of SnS2and SnSe2. *Physical Review, 178*(3), 1279-1283. doi:10.1103/physrev.178.1279

[74] Fong, C. Y., & Cohen, M. L. (1973). Electronic Energy Band Structure of SnS2 and SnSe2. *Physical Review B, 7*(10), 4748-4748. doi:10.1103/physrevb.7.4748

[75] Fong, C. Y., & Cohen, M. L. (1973). Electronic Energy Band Structure of SnS2and SnSe2. *Physical Review B, 7*(10), 4748-4748. doi:10.1103/physrevb.7.4748

[76] Schlüter, M., & Cohen, M. L. (1976). Valence-band density of states and chemical bonding for several non-transition-metal layer compounds: SnSe2, PbI2, BiI3, and GaSe. *Physical Review B, 14*(2), 424-431. doi:10.1103/physrevb.14.424

[77] Aymerich, F., Meloni, F., & Mula, G. (1973). Pseudopotential band structure of solid solutions SnSxSe2−x. *Solid State Communications, 12*(2), 139-141. doi:10.1016/0038-1098(73)90523-1

[78] Bordas, J., Robertson, J., & Jakobsson, A. (1978). Ultraviolet properties and band structure of SnS2, SnSe2, CdI2, PbI2, BiI3and BiOI crystals. *Journal of Physics C: Solid State Physics, 11*(12), 2607-2621. doi:10.1088/0022-3719/11/12/021

[79] Qian, X., Wu, H., Wang, D., Zhang, Y., Wang, J., Wang, G., . . . Zhao, L. (2019). Synergistically optimizing interdependent thermoelectric parameters of n-type PbSe through alloying CdSe. *Energy & Environmental Science, 12*(6), 1969-1978. doi:10.1039/c8ee03386b

[80] Liu, W., Yan, X., Chen, G., & Ren, Z. (2012). Recent advances in thermoelectric nanocomposites. *Nano Energy, 1*(1), 42-56. doi:10.1016/j.nanoen.2011.10.001

[81] Liu, W., Tan, X., Yin, K., Liu, H., Tang, X., Shi, J., . . . Uher, C. (2012). Convergence of Conduction Bands as a Means of Enhancing Thermoelectric Performance ofn-TypeMg2Si1−xSnxSolid Solutions. *Physical Review Letters*, *108*(16). doi:10.1103/physrevlett.108.166601

[82] Guan, X., Lu, P., Wu, L., Han, L., Liu, G., Song, Y., & Wang, S. (2015). Thermoelectric properties of SnSe compound. *Journal of Alloys and Compounds*, *643*, 116-120. doi:https://doi.org/10.1016/j.jallcom.2015.04.073

[83] Cheng, L., Chen, Z., Yang, L., Han, G., Xu, H., Snyder, G. J., . . . Zou, J. (2013). T-Shaped Bi2Te3–Te Heteronanojunctions: Epitaxial Growth, Structural Modeling, and Thermoelectric Properties. *The Journal of Physical Chemistry C, 117*(24), 12458-12464. doi:10.1021/jp4041666

[84] Zhu, T., Liu, Y., Fu, C., Heremans, J. P., Snyder, J. G., & Zhao, X. (2017). Compromise and Synergy in High-Efficiency Thermoelectric Materials. *Advanced Materials, 29*(30). doi:10.1002/adma.201702816

[85] Fu, J., Su, X., Xie, H., Yan, Y., Liu, W., You, Y., . . . Tang, X. (2018). Understanding the combustion process for the synthesis of mechanically robust SnSe thermoelectrics. *Nano Energy*, *44*, 53-62. doi:10.1016/j.nanoen.2017.11.073

[86] Ishida, A., Thao, H. T., Nakashima, S., Yamamoto, H., & Ishikiriyama, M. (2018). Thermoelectric properties of PbTe films and PbTe-based superlattices. *Materials Today: Proceedings*, *5*(4), 10187-10194. doi:10.1016/j.matpr.2017.12.264

[87] Liang, B., Song, Z., Wang, M., Wang, L., & Jiang, W. (2013). Fabrication and Thermoelectric Properties of Graphene/Bi2Te3Composite Materials. *Journal of Nanomaterials*, *2013*, 1-5. doi:10.1155/2013/210767

[88] Paredes, J. I., Villar-Rodil, S., Martínez-Alonso, A., & Tascón, J. M. (2008). Graphene Oxide Dispersions in Organic Solvents. *Langmuir, 24*(19), 10560-10564. doi:10.1021/la801744a

[89] Kavinkumar, T., Sastikumar, D., & Manivannan, S. (2015). Effect of functional groups on dielectric, optical gas sensing properties of graphene oxide and reduced graphene oxide at room temperature. *RSC Advances, 5*(14), 10816-10825. doi:10.1039/c4ra12766h

[90] Ray, S. C., Bhunia, S. K., Saha, A., & Jana, N. R. (2015). Graphene oxide (GO)/reduced-GO and their composite with conducting polymer nanostructure thin films for non-volatile memory device. *Microelectronic Engineering, 146*, 48-52. doi:10.1016/j.mee.2015.04.001

[91] Lu, G., Ocola, L. E., & Chen, J. (2009). Reduced graphene oxide for room-temperature gas sensors. *Nanotechnology, 20*(44), 445502. doi:10.1088/0957-4484/20/44/445502

[92] Schrade, M., Fjeld, H., Norby, T., & Finstad, T. G. (2014). Versatile apparatus for thermoelectric characterization of oxides at high temperatures. *Review of Scientific Instruments, 85*(10), 103906. doi:10.1063/1.4897489

[93] Pham, A., Vu, T. H., Cheng, C., Trinh, T. L., Lee, J., Ryu, H., . . . Cho, S. (2020). High-Quality SnSe2 Single Crystals: Electronic and Thermoelectric Properties. *ACS Applied Energy Materials, 3*(11), 10787-10792. doi:10.1021/acsaem.0c01846

[94] LFA 457 MicroFlash®. (n.d.). Retrieved from https://www.netzsch-thermal-analysis.com/en/products-solutions/thermal-diffusivity-conductivity/lfa-457-microflash/

[95] Deepak, D., Saurabh, D., & Agarwal, R. (2020, November 20). Validation of the UV – Visible spectrophotometer. Retrieved from https://lab-training.com/2015/07/14/validation-of-the-uv-visible-spectrophotometer/

[96] Hall Effect Measurement System. (n.d.). Retrieved from https://www.magnetic-instrument.com/hall-effect-system.htm

[97] Renewable Energy Statistics 2017. (n.d.). Retrieved from https://www.irena.org/publications/2017/Jul/Renewable-Energy-Statistics-2017

[98] X-ray diffraction (XRD). (n.d.). Retrieved from https://www.rigaku.com/zh-hans/node/713

[99] JEOL JSM-6490LV SEM. (2020, May 14). Retrieved from https://www.semtechsolutions.com/product/jeol-jsm-6490lv-sem/